Mode I+III multiscale cohesive zone model with facet coarsening and overlap: Solutions and applications to facet orientation and toughening

V. Lazarus, B. Prabel, T. Cambonie, J.B. Leblond

Mode I+III multiscale cohesive zone model with facet coarsening and overlap: Solutions and applications to facet orientation and toughening

V. Lazarus[1], B. Prabel[1,2], T. Cambonie[3], J.B. Leblond[4]

[1] *IMSIA, CNRS, EDF, CEA, ENSTA Paris, Institut Polytechnique de Paris, 828 bd des Maréchaux, 91762 Palaiseau cedex, France*

[2] *Den-Service d'études mécaniques et thermiques (SEMT), CEA, Université Paris-Saclay, F-91191, Gif-sur-Yvette, France*

[3] *Laboratoire FAST, Univ. Paris-Sud, CNRS, Université Paris-Saclay, F-91405, Orsay, France*

[4] *Sorbonne Université, Faculté des Sciences et Ingénierie, Campus Pierre et Marie Curie, CNRS, UMR 7190, Institut Jean Le Rond d'Alembert, F-75005 Paris, France*

Abstract

When subjected to some anti-plane shear mode III loading, segmentation of the crack front frequently occurs during propagation: even if the crack is initially planar, propagation produces facets/segments rotated toward the shear free direction. These facets induce some modifications in the local loading of the crack tips that can be captured through the multi-scale cohesive zone model proposed by Leblond et al., 2015. Assuming that the width of the facets is small in comparison to their length, the facets can be considered at the microscale, as a bidimensional periodic array of tilted cracks perpendicularly to the direction of propagation, and at the macroscale, as a growing Cohesive Zone. The model was developed initially supposing a constant period, small tilt angles and non-overlapping facets. The first aim of this paper is to relax these assumptions to deal with more realistic cases. For this, the microscale problem is solved using XFEM and the outputs are further incorporated into the model to get some results on the macroscale, in particular the effective fracture energy. The second objective is to introduce some experiments to show the relevance of the assumptions made and to demonstrate the ability of the approach (i) to determine the inclination of the facets and (ii) to quantify, in both fatigue and brittle fracture, the toughening due to the decrease of the crack opening driven by the unbroken ligaments between the facets.

Keywords: Brittle fracture, Mode I+III, Tilted facets, Multiscale Cohesive Zone model, Effective Fracture Resistance

In the context of Linear Elastic Fracture Mechanics (LEFM), the behaviour of a crack loaded in modes I and II is nowadays generally well understood (Erdogan and Sih, 1963; Leblond and Torlai, 1992; Flores and Xu, 2013; Pham et al., 2017). However, adding some mode III contribution greatly complicates the problem, since segmentation of the crack front (Fig. 1) frequently occurs during propagation (Sommer, 1969; Hull, 1995; Lazarus et al., 2008): even if the crack is initially planar and its front straight, propagation produces segments rotated toward the shear free direction. Two situations may occur: either the segments

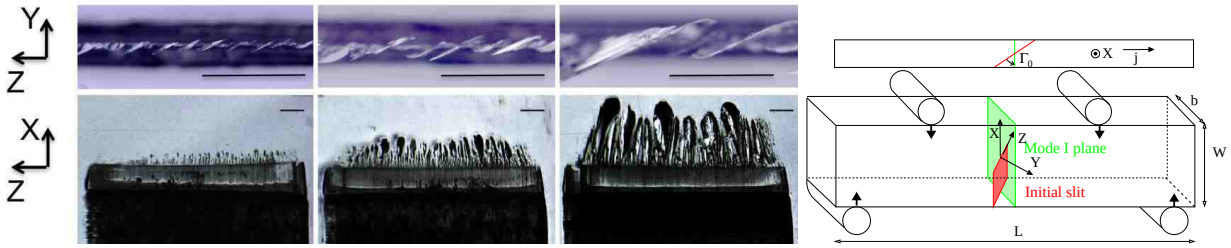

Figure 1: Segmentation, facet coarsening and overlap observed by transparency in fatigue bending experiments performed on plexiglass ($W = b = 10$ mm, $L = 50$ mm, $\Gamma_0 = 30^0$). The advance is driven by a given constant mean force and amplitude. Each column corresponds to a given number of loading cycles, which increases from the left to the right. The first row are top views (in the $X-$direction), the initial slit appears dark and blurred in the background and the facets clear and sharp in the foreground. The second row are front views (in the $Y-$direction), the initial slit (black rectangle at the bottom) propagates upwards. In all these pictures, $\beta \equiv K_{III}^{(0)}/K_I^{(0)} \simeq 0.3$ along the initial slit. The bar scales are all 1 mm. Rough estimates deduced from these digital pictures give $\eta \sim 0.2$, $\alpha \sim 27$ degrees (see Fig. 2 for notations).

(also termed facets) are formed by nucleation of new isolated cracks along the initial slit (Palaniswamy and Knauss, 1975; Chen et al., 2015; Pham and Ravi-Chandar, 2016), or their rotation is progressive (Sommer, 1969). Coarsening of the facets (see Fig. 1), with merging of facets resulting in period doubling, is also a usual observation (Goldstein and Osipenko (2012); Chen et al. (2015); Pham and Ravi-Chandar (2016) for instance). Initially, the segments or facets are not linked to each other. The connection between them forms only in a second phase, through development of a saw-tooth factory roof pattern, with $A-$zones (Fig. 2) corresponding to the initial facets and $B-$zones between them forming steps or 'river lines'. Crack propagation is more energetically favoured along $A-$zones than along $B-$zones, whose propagation is thus delayed (Lazarus et al., 2001a). This segmentation phenomenon occurs from the millimeter (Lazarus et al., 2008) to the kilometer scales (Pollard et al., 1982), in many types of materials ranging from metals (Eberlein et al., 2017), to polymers (Wu, 2006; Lazarus et al., 2008; Lin et al., 2010; Chen et al., 2015), glass (Sommer, 1969), cheese (Goldstein and Osipenko, 2012), soft matter (Ronsin et al., 2014) and rocks (Pollard et al., 1982). This suggests it must have a quite universal explanation at the continuum scale. Segmentation has implications on lifetime predictions in engineering: turbines (Flavien, 2012), railways (Bonniot et al., 2018) or on the shape of stick-slip faults (Cambonie et al., 2019).

From a theoretical point of view, the geometry resulting from crack propagation is inherently 3D, which highly complicates the theoretical treatment (Lazarus et al., 2001a,b; Gravouil et al., 2002). Phase-field simulations have shown (Pons and Karma, 2010) that in the absence of mode II but presence of mode III, straight propagation is not the only solution satisfying both Griffith (1920)'s energetic condition and the Principle of Local Symmetry (PLS, stating that $K_{II} = 0$ during propagation (Goldstein and Salganik, 1974)): A bifurcated solution with a helical front is more likely to occur. This led us to perform a linear stability

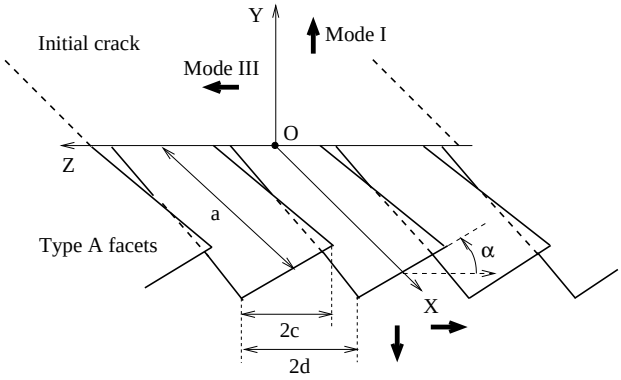

Figure 2: Schematic view of the formation of facets (A-zones) in mode I+III and associated notations. Coalescence (or coarsening) results in an increase of d with a (not represented on the figure for legibility).

analysis (Leblond et al., 2011) that evidenced a lower bound for the instability on the ratio $K_{III}^{(0)}/K_I^{(0)}$ of the mode III to mode I initial stress intensity factors. Finally, a non-linear stability analysis using a phase-field method has highlighted the subcritical character of the bifurcation (Chen et al., 2015), meaning that even below the linear analysis threshold, the instability may be initiated by some imperfections of sufficiently large amplitude (Leblond and Lazarus, 2015). This rationalizes the fact that segmentation is generally observed below the linear stability threshold (Pham and Ravi-Chandar, 2014), with a few exceptions however (Ronsin et al., 2014; Eberlein et al., 2017). The question of the instability onset is not definitively settled, but may be correlated to the 'level' of imperfections in the experiments (linked to the sharpness of the initial slit, material inhomogeneities, fluctuations in the loading...).

The shape of the facets may be quantified through the evolution along the propagation direction X of (i) the rotation angle of the facets α, (ii) the slenderness ratio $\eta = d/a$, (iii) the relative lateral extension c/d (see Fig. 2). At initiation, α has been verified experimentally to correspond (Pham and Ravi-Chandar, 2016) to the shear free plane defined by the angle (Cooke and Pollard, 1996):

$$\alpha_0 = \frac{1}{2} \arctan \left[\frac{K_{III}^{(0)}}{\left(\frac{1}{2} - \nu\right) K_I^{(0)}} \right] \tag{1}$$

Due to mutual interactions, further propagation of the facets leads to a different steady-state angle (Chen et al., 2015)[1]. This angle can be determined by numerical means (Chen et al., 2015) or using a perturbation approach, assuming the length of the facets to be much larger than their width (Leblond et al., 2019). This approach leads to:

$$\alpha = \frac{K_{III}^{(0)}}{K_I^{(0)}(1 - 5\nu/4)}, \text{ if } \frac{K_{III}^{(0)}}{K_I^{(0)}} \ll 1 \tag{2}$$

[1] still denoted α for the sake of simplicity.

When coalescence of the facets occurs, the slenderness ratio $\eta = d/a$ corresponds also to the coalescence rate. The values of η obtained by numerical simulations (Chen et al., 2015) has been verified to be in agreement with experiments via some ajustable parameter whose physical origin has not yet been studied. The evolution of the lateral extension c/d is complex since it results from the 3D propagation of the facets, including the most advanced and lateral parts, which moreover depends on the mutual interactions between the facets leading to the characteristic en-passant handshaking S-shape (see Melin (1983); Hull (1995); Ghelichi and Kamrin (2015) and supplemental material of Chen et al. (2015)).

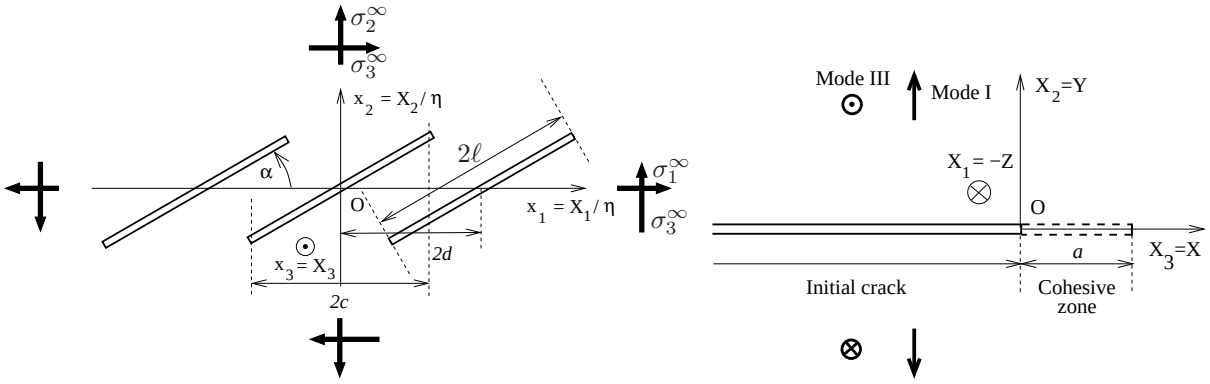

(a) Internal or inner problem at the microscale.

(b) External or outer problem at the macroscale

Figure 3: Multiscale cohesive zone model: decomposition of the initial 3D problem (Fig. 2) in two 2D problems: at the microscale, the facets appear as an array of parallel cracks subjected to remote stresses; at the macroscale, they are embedded in a cohesive zone.

Segmentation leads to partial breaking of the material, hence to a decrease of the energy available to propagate the crack (Hull, 1993) and consequently to an increase of the apparent fracture toughness. Toughening due to segmentation can also be observed during transgranular fracture in bycristals where twisted segments are formed along the weakest interfaces (Wei et al., 2009), with the main difference that segmentation is not triggered here by any material anisotropy, but by the sole presence of mode III in an otherwise isotropic and homogeneous material.

This toughening effect induced by the unbroken ligaments between the facets can be quantified by the multi-scale Cohesive Zone (CZ) model developed by Leblond et al. (2015). Assuming that the slenderness of the facets η is small, the facets can be considered as a bidimensional periodic array of tilted cracks at the microscale (internal problem, fig. 3(a)) and as a growing CZ at the macroscale (external problem, Fig. 3(b)). Both problems are linked through some scaling up of the CZ at the macroscale, via the small parameter η: the remote displacements and stresses in the internal problem are related to the displacements and stresses on the CZ in the external problem. Thus the relation between the remote displacements and stresses in the internal problem yields a similar relation between the components of the displacement discontinuity and the

stresses on the CZ in the external problem. This relation depends on the geometry of the facets, through the elastic compliance induced by the periodic array of cracks. From there, it is possible to determine some properties about the propagation (i) of the periodic array of cracks at the microscale (Fig. 3(a)); (ii) of the CZ at the macroscale (Fig. 3(b)).

In our paper of 2015, the period d of the array of facets was supposed to be independent of the distance of propagation a. This led to a decrease of the effective energy release rate with the crack advance a, implying that the loading has to be increased in order to maintain propagation of the crack. This is in contradiction with experiments where (i) coalescence usually occurs (Chen et al., 2015; Pham and Ravi-Chandar, 2016) and (ii) self-sustained propagation under constant loading is observed. This led Leblond et al. (2015) to extend the CZ model to deal with a d growing proportionally to a, in order to model coalescence and coarsening of facets (see their Eq. 52). But at that time, the method was only sketched and neither solutions, nor applications were presented. Moreover, only small rotation angles or small c/d ratios were considered, relying on some approximate solution of the internal 2D problem provided by Leblond and Frelat (2014).

In the present paper, we aim at solving the equations including coalescence of facets given in Leblond et al. (2015) (Eq. 52) for both large angles and large c/d ratios, including the possibility of crack overlaps (corresponding to $c/d > 1$). Such situations are currently observed in experiments as illustrated in Fig. 1 and in §1. For this purpose, it is necessary first to solve the internal problem for the case with overlaps, since it has not been done previously. Details about the method are given in Appendix A and the main results in §2. Second (§3), this new solution is incorporated into the model, in particular to compute the effective fracture energy at the macroscale. Finally, we will show how the model can be used to determine the steady-state angle of inclination of the facets (§4), and to quantify the toughening due to the presence of the facets (§5) in both fatigue (under cyclic loading), where it results in a decrease of the crack advance rate, and brittle fracture, where it results in an increase of Griffith's fracture threshold; the assumptions of the approach being justified and the results being discussed in light of the bending experiments presented in §1.

1. Four Points Bending (4PB) experiments

The experiments of Fig. 1 will be used to show the relevance of the model's assumptions and to illustrate the comparison with the theoretical results[2]. The samples are beams (dimensions 10 mm×10 mm×50 mm) made of cast[3] plexiglass ($\nu \sim 0.4$, $E \sim 3$ GPa), containing an inclined initial slit (depth $\sim 2-3$ mm, $\Gamma_0 = 10$,

[2]The scope of this paper being rather theoretical, only rough results will be given here without error bars and discussions of the tricky numerical and experimental methods involved, for instance to measure α (Cambonie and Lazarus, 2014). More extensive and accurate comparisons will be the topic of a future, more experimentally oriented publication.

[3]Not extruded, to ensure isotropy of the material.

20, 30°) prepared as explained in Chen et al. (2015). Progressive crack propagation is achieved through cyclic fatigue loading in a 4 Points Bending (4PB) testing machine, varying the applied force P around a mean value P_0, with a fixed amplitude ΔP. Both $K_{III}^{(0)}$ and $K_I^{(0)}$ are then proportional to P so that the mode mixity $\beta \equiv \frac{K_{III}^{(0)}}{K_I^{(0)}}$ is constant during the whole experiment. In these experiments, β is approximately linked to the angle Γ_0 through the formula $\beta = \frac{1}{2}\tan\Gamma_0$ (Pook, 1995; Lazarus et al., 2008; Lin et al., 2010). The three columns of Fig. 1 correspond to three different similar specimens having $\Gamma_0 = 30°$, where the crack was stopped at different stages of the propagation. Several visual observations can be made on these pictures: while the front is initially straight, it segments into facets, that further coalesce and the shape of the facets is elongated.

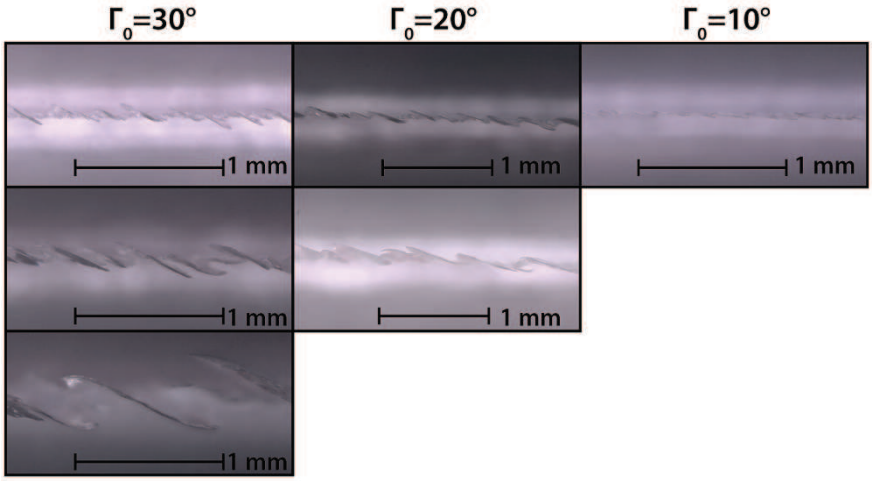

Figure 4: Top views of several partially broken fatigue samples. Each "line" (horizontal set of pictures) corresponds to different stages of propagation, each "column" (vertical set of pictures) to different values of Γ_0.

Fig. 4 gathers the top views of the crack obtained in some other experiments performed for $\Gamma_0 = 10°$ and 20°. Rough estimates of the coalescence rate η and the rotation angle α can be obtained from direct measurements on the pictures. The coalescence rate is estimated to be $\eta \sim 0.2$ for all inclinations of the initial slit considered, in line with the model's assumption of small η. The angle α is observed to be nearly

Γ_0	10°	20°	30°
α Experiments	12°	20°	27°
α Eq. 2	10°	21°	33°
α Eq. 1	20.7°	30.6°	35.4°

Table 1: Experimental values of α and predictions of Eqs. 2 and 1 for $\nu = 0.4$ and $\beta = \frac{\tan\Gamma_0}{2}$.

constant and its value is gathered in Table 1 for different values of Γ_0 together with the predictions of Eqs. 2 and 1 taking $\nu = 0.4$. As anticipated in the introduction, Eq. 1, even if valid at initiation (Pham and Ravi-Chandar, 2016), overestimates the steady-state value of the angle measured here[4]. In contrast, Eq. 2 which was derived for the steady-state situation assuming the facets to be shear-free (Leblond et al., 2019), is in excellent agreement with the experiments, especially in its domain of validity, that is for small values of β or Γ_0. This nice result should however be taken with caution, since formulas (Eq. 2) and (Eq. 1) are very sensitive to the precise value of ν, and polymers like plexiglass (i) exhibit some viscoelastic behaviour which contradicts our hypothesis of pure elasticity, and sheds some doubts on the values of the elastic constants; and (ii) present crack morphologies which are sensitive to the cyclic load history (Pulos and Knauss, 1998). A more systematic and extensive study is required to conclude.

Meanwhile, guided by those experimental observations, our model is derived under the following assumptions: linear isotropic elasticity, initial straight crack under mode I+III loading, formation of straight elongated facets, yielding small values of η, which coalesce during propagation. An additional assumption is to focus on the propagation in the vicinity of the initial crack, in which the loading mixity β can be considered to be constant, and the shape of the facet to stay stationary perpendicularly to the propagation direction, so that α and η can be assumed to be constant. The assumption of small η permits to uncouple the nominally 3D problem (fig. 2) in two 2D ones (fig. 3): an internal one corresponding to an array of parallel inclined cracks in a plane orthogonal to the propagation direction (described in §2) and an external one where the facets are embedded in a straight Cohesive Zone extension (detailed in §3).

2. Internal problem at the scale of the facets

2.1. The equations

Like in Fig. 3(a), consider an array of parallel tilted cracks, embedded in a linear elastic isotropic material (E denotes Young's modulus and ν Poisson's coefficient), loaded by the remote stresses

$$\sigma_1^\infty = \sigma_{11}^\infty, \quad \sigma_2^\infty = \sigma_{22}^\infty, \quad \sigma_3^\infty = \sigma_{12}^\infty$$

(with Voigt-like notations). This geometry is characterized by two dimensionless parameters: α, the tilt angle of the facets and c/d, the overlap ratio[5]. Thanks to the linearity of the elasticity problem, the stress

[4]This conclusion unfortunately relies on two distinct experiments, since we are not able to measure α continuously from the initiation to the steady-state in our experiments.

[5]Rigorously speaking, c and d designate the projected width of the facets and the period in the *external* problem. The projected width and period in the *internal* problem, considered here, are deduced from those in the external problem through multiplication by some large factor, and should be noted differently, for instance $\bar{c}$ and $\bar{d}$ as was done by Leblond et al. (2015). They are renoted c and d here for simplicity, this slight inaccuracy of notation being tolerable since the overlap ratio may indifferently be defined as c/d or $\bar{c}/\bar{d}$.

intensity factors k_p, $p = I$, II at the lateral crack tips can be expressed under the following form[6]:

$$k_p \equiv \sqrt{2d}\,\mathcal{F}_\lambda^p\left(\frac{c}{d}\,,\alpha\right)\sigma_\lambda^\infty \tag{3}$$

where Einstein's implicit summation convention has been used for the index $\lambda = 1, 2, 3$. Noteworthy is the independence of the functions $\mathcal{F}_\lambda^p$ with E and ν; the first property is an obvious consequence of homogeneity considerations, and the second results from a general theorem of Muskhelishvili (1953).

2.2. Some results

The approximate expressions of the functions $\mathcal{F}_\lambda^p(c/d\,,\alpha)$ proposed by Leblond and Frelat (2014) are as follows:

$$\left\{\begin{array}{l}
\mathcal{F}_1^I\left(\dfrac{c}{d},\,\alpha\right) \simeq \sqrt{\tan\left(\dfrac{\pi c}{2d}\right)}\dfrac{1-\cos(2\alpha)}{2\sqrt{\cos\alpha}} \quad ; \quad \mathcal{F}_2^I\left(\dfrac{c}{d},\,\alpha\right) \simeq \sqrt{\tan\left(\dfrac{\pi c}{2d}\right)}\dfrac{1+\cos(2\alpha)}{2\sqrt{\cos\alpha}} \quad ; \\
\mathcal{F}_3^I\left(\dfrac{c}{d},\,\alpha\right) \simeq -\sqrt{\tan\left(\dfrac{\pi c}{2d}\right)}\left[3+\dfrac{\pi c/d}{\sin(\pi c/d)}\right]\dfrac{\sin(2\alpha)}{4\sqrt{\cos\alpha}} \quad ; \\
\mathcal{F}_1^{II}\left(\dfrac{c}{d},\,\alpha\right) \simeq -\sqrt{\tan\left(\dfrac{\pi c}{2d}\right)}\dfrac{\sin(2\alpha)}{2\sqrt{\cos\alpha}} \quad ; \quad \mathcal{F}_2^{II}\left(\dfrac{c}{d},\,\alpha\right) \simeq \sqrt{\tan\left(\dfrac{\pi c}{2d}\right)}\left[3-\dfrac{\pi c/d}{\sin(\pi c/d)}\right]\dfrac{\sin(2\alpha)}{4\sqrt{\cos\alpha}} \quad ; \\
\mathcal{F}_3^{II}\left(\dfrac{c}{d},\,\alpha\right) \simeq \sqrt{\tan\left(\dfrac{\pi c}{2d}\right)}\dfrac{\cos(2\alpha)}{\sqrt{\cos\alpha}}\,.
\end{array}\right. \tag{4}$$

Comparisons with the results of some finite element calculations (Leblond and Frelat, 2014) have shown that these formulae yield quite acceptable results except when α and c/d are simultaneously large. To extend them to larger values of α and c/d (including overlaps), we have used a XFEM method coupled with hierarchical mesh refinement whose application to non-linear fatigue crack propagation can be found in Gibert et al. (2019). Values of the functions $\mathcal{F}_\lambda^p$ are computed from $\alpha = 0$ to $\alpha = 45°$ with a step of 2.5°, and for $c/d = 0.1$ to 1.4 with a step of 0.2. To avoid intersecting cracks, the range of α is limited to $\alpha \geq 5°$ for $\frac{c}{d} \geq 1$. Details about the method are given in Appendix A. The results are reported in Fig. 5 where the $\mathcal{F}_\lambda^p$ are plotted as functions of c/d for several values of α. As expected the numerical results (plotted with discrete dots) are in agreement with the approximate expressions (Eq. 4, plotted with full lines) as long as c/d is small enough, the validity range decreasing with increasing α.

One also notices that $|\mathcal{F}_\lambda^p|$ increases with c/d in all cases, except for $p = II$ and large enough values of c/d, so that stability of the straight lateral propagation, once the Griffith or Irwin propagation threshold is reached, is unlikely despite some foreseeable screening effect (Leblond et al., 2015): at some point, the facets will probably link up, forming the characteristic en-passant handshaking shape (Melin, 1983; Hull, 1995). Another remarkable point is that the functions $\mathcal{F}_2^{II}$ and $\mathcal{F}_3^{II}$ providing the mode II stress intensity

[6]Notice that the notations are slightly different from those in Leblond et al. (2015): the factor $\sqrt{\tan\left(\frac{\pi c}{2d}\right)}$ has been removed here since it was limiting the possible range of the ratio c/d to values smaller than 1. Accordingly we have slightly changed the notation, moving from F_λ^p to $\mathcal{F}_\lambda^p$.

factor may be positive or negative, meaning that the branches may attract or repulse each other (Schwaab et al., 2018).

3. External problem at the macroscale

Now, zooming out, the internal problem (Fig. 3(a)) becomes the external problem (Fig. 3(b)) where the array of facets is embedded in a cohesive zone. With regard to the dependence of the facet geometry with X, we suppose that (i) c/d and α are independent of X, but (ii) as discussed in the Introduction, the spacing d between the facets scales with X:

$$d(X) = \eta X \tag{5}$$

where η is a constant. This relation remains true at the tip $X = a$, so that $\eta = d(a)/a$. The parameter η is connected to the coalescence rate. We also assume that the mode mixity β remains constant during propagation, that is does not depend on X.

Matched asymptotic expansions using the small parameter η are used to link the internal and external problems. Details of the method are rather complex and given in Leblond et al. (2015). Here, we just recall the general lines of the reasoning and main equations.

3.1. The equations

The solution of the internal problem yields the relations between the far displacements and stresses, accounting for the presence of the periodic array of cracks. But the matched asymptotic expansions permit to relate these quantities to the displacements and stresses on the cohesive zone in the external problem; whence the relation between the latter displacements and stresses.

Denote $\mathbf{U}$ and $\mathbf{\Sigma}$ the displacement vector and stress tensor in the external problem. At a point X along the cohesive zone, the displacement jump $[\![\mathbf{U}]\!](\mathbf{X})$ and the stress $\mathbf{\Sigma}(X) \equiv \mathbf{\Sigma}(X, Y = 0)$ are linked by:

$$\left\{\begin{array}{lcl} [\![U_X]\!](X) & = & 0 \\ [\![U_Y]\!](X) & = & \dfrac{4(1-\nu^2)d}{E}\left[\mathcal{A}_{22}\Sigma_{YY}(X) + \mathcal{A}_{12}\Sigma_{ZZ}(X) - \mathcal{A}_{23}\Sigma_{YZ}(X)\right] \\ [\![U_Z]\!](X) & = & \dfrac{4(1-\nu^2)d}{E}\left[-\mathcal{A}_{23}\Sigma_{YY}(X) - \mathcal{A}_{13}\Sigma_{ZZ}(X) + \mathcal{A}_{33}\Sigma_{YZ}(X)\right]. \end{array}\right. \tag{6}$$

The quantities $\mathcal{A}_{\lambda\mu}$ and Σ_{ij} here depend on the geometry of the array of facets. More precisely:

- The quantities $\mathcal{A}_{\lambda\mu}$ are related to the functions $\mathcal{F}^p_\lambda$ and $\mathcal{F}^p_\mu$ (defined by Eq. 3) through the relation:

$$\mathcal{A}_{\lambda\mu} \equiv \mathcal{A}_{\lambda\mu}(c/d, \alpha) \equiv \frac{1}{\cos\alpha}\int_0^{c/d} \mathcal{F}^p_\lambda(x, \alpha)\, \mathcal{F}^p_\mu(x, \alpha)\, \mathrm{d}x. \tag{7}$$

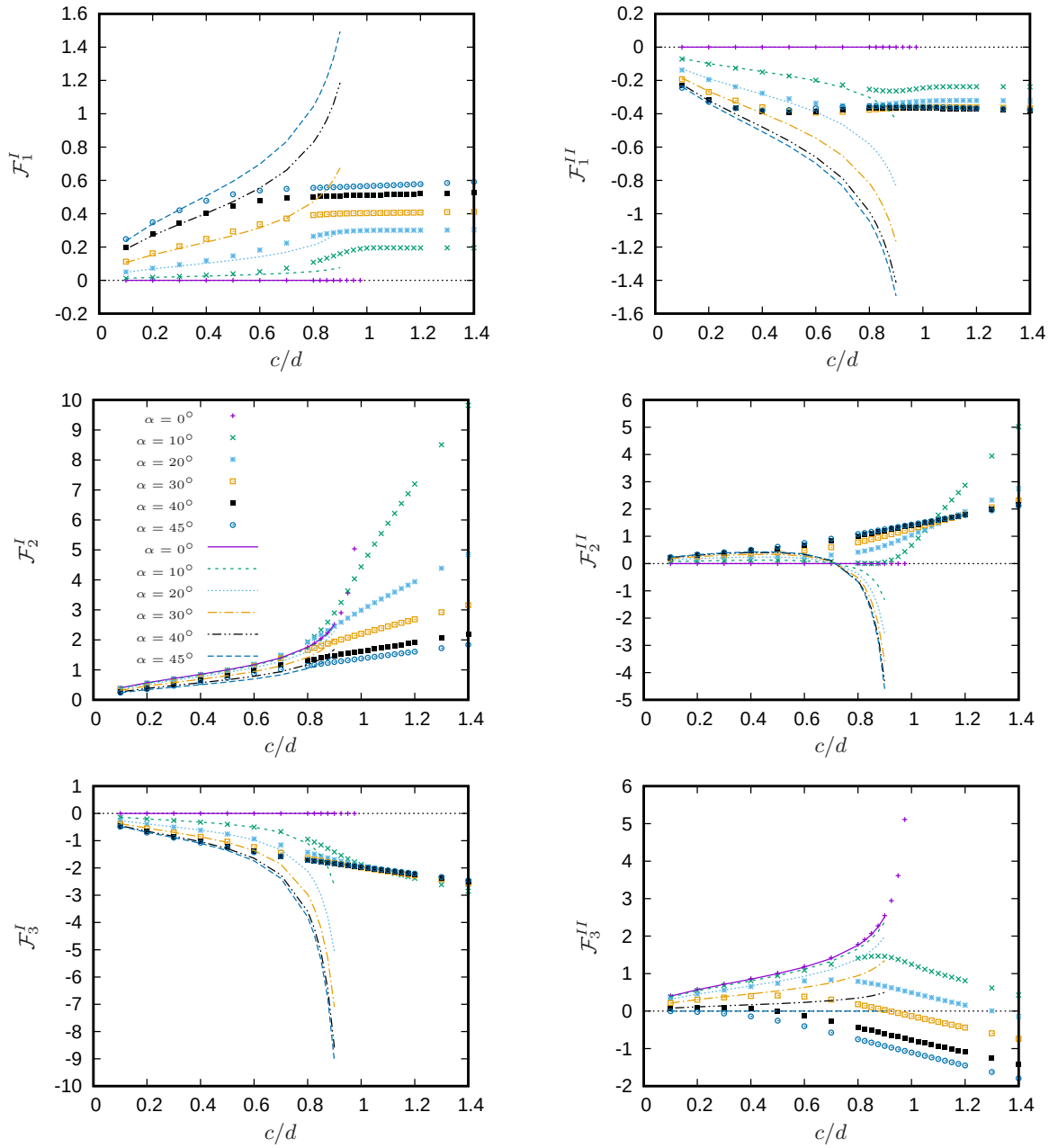

Figure 5: Functions $\mathcal{F}_i^k\left(\alpha, \frac{c}{d}\right)$ defined in Eq. 3. Solid lines corresponds to the asymptotic values (Eq. 4) and points to the values obtained by XFEM. The symbols are the same for all graphs and are defined once and for all, in the figure showing $\mathcal{F}_2^I(c/d)$.

- The stress tensor $\mathbf{\Sigma}(X)$ is linked to that in the vicinity of the initial crack tip without facets, that is to the initial stress intensity factors $K_I^{(0)}$ and $K_{III}^{(0)}$, reduced by some additional surface tractions $\pm[p(X)\,\mathbf{e}_Y + q(X)\,\mathbf{e}_Z]$ exerted on the faces of the cohesive zone, resulting from partial opening of this zone (hindered by the unbroken ligaments between the facets):

$$\left\{\begin{array}{lcll} \Sigma_{YY}(X) & = & \Sigma_{XX}(X) & = & \dfrac{K_I^{(0)}}{\sqrt{2\pi X}} - p(X) \\ \Sigma_{ZZ}(X) & = & \nu\,[\Sigma_{XX}(X) + \Sigma_{YY}(X)] & = & 2\nu\left[\dfrac{K_I^{(0)}}{\sqrt{2\pi X}} - p(X)\right] \\ \Sigma_{YZ}(X) & & & = & \dfrac{K_{III}^{(0)}}{\sqrt{2\pi X}} - q(X). \end{array}\right. \tag{8}$$

But on the other hand these additional tractions generate a displacement discontinuity across the faces of the CZ obeying the classical LEFM formulae

$$\left\{\begin{array}{lcl} \dfrac{\mathrm{d}[\![U_Y]\!]}{\mathrm{d}X}(X) & = & \dfrac{4(1-\nu^2)}{\pi E}\,PV\displaystyle\int_0^a p(X')\sqrt{\frac{a-X'}{a-X}}\,\frac{\mathrm{d}X'}{X'-X} \\ \dfrac{\mathrm{d}[\![U_Z]\!]}{\mathrm{d}X}(X) & = & \dfrac{4(1+\nu)}{\pi E}\,PV\displaystyle\int_0^a q(X')\sqrt{\frac{a-X'}{a-X}}\,\frac{\mathrm{d}X'}{X'-X}\,. \end{array}\right. \tag{9}$$

Differentiating Eqs. 6 with respect to X, eliminating $\frac{\mathrm{d}[\![U_Y]\!]}{\mathrm{d}X}$ and $\frac{\mathrm{d}[\![U_Z]\!]}{\mathrm{d}X}$ between the result and Eqs. 9, and accounting for the expressions of the stresses Σ_{YY}, Σ_{ZZ}, Σ_{YZ} given by Eq. 8, one gets the following integral equations on the unknown tractions p and q:

$$\left\{\begin{array}{l} (\mathcal{A}_{22}+2\nu\mathcal{A}_{12})\left(\dfrac{\mathrm{d}p}{\mathrm{d}X}+\dfrac{p}{X}\right) - \mathcal{A}_{23}\left(\dfrac{\mathrm{d}q}{\mathrm{d}X}+\dfrac{q}{X}\right) \\ \quad + \dfrac{1}{\pi\eta X}\,PV\displaystyle\int_0^a p(X')\sqrt{\frac{a-X'}{a-X}}\,\frac{\mathrm{d}X'}{X'-X} \\ \qquad = \dfrac{(\mathcal{A}_{22}+2\nu\mathcal{A}_{12})K_I^{(0)} - \mathcal{A}_{23}K_{III}^{(0)}}{2\sqrt{2\pi}\,X^{3/2}} \\ -(\mathcal{A}_{23}+2\nu\mathcal{A}_{13})\left(\dfrac{\mathrm{d}p}{\mathrm{d}X}+\dfrac{p}{X}\right) + \mathcal{A}_{33}\left(\dfrac{\mathrm{d}q}{\mathrm{d}X}+\dfrac{q}{X}\right) \\ \quad + \dfrac{1}{\pi(1-\nu)\eta X}\,PV\displaystyle\int_0^a q(X')\sqrt{\frac{a-X'}{a-X}}\,\frac{\mathrm{d}X'}{X'-X} \\ \qquad = -\dfrac{(\mathcal{A}_{23}+2\nu\mathcal{A}_{13})K_I^{(0)} - \mathcal{A}_{33}K_{III}^{(0)}}{2\sqrt{2\pi}\,X^{3/2}}\,. \end{array}\right. \tag{10}$$

Moreover, the boundary conditions $[\![U_Y]\!](a) = [\![U_Z]\!](a) = 0$ of closure at the tip of the cohesive zone yield, with Eqs. 6 and 8:

$$\left\{\begin{array}{lcl} p(a) & = & \dfrac{K_I^{(0)}}{\sqrt{2\pi a}} \\ q(a) & = & \dfrac{K_{III}^{(0)}}{\sqrt{2\pi a}}\,. \end{array}\right. \tag{11}$$

Once the tractions p, q are known by solving Eq. 10 with the boundary conditions (Eq. 11), the macroscopic or effective stress intensity factors at the tip of the CZ (that is in fact on a line connecting the facet tips) can be obtained through the formulae:

$$\left\{\begin{array}{lcl} K_I &=& \sqrt{\dfrac{2}{\pi}}\displaystyle\int_0^a p(X)\frac{\mathrm{d}X}{\sqrt{a-X}} \\ K_{III} &=& \sqrt{\dfrac{2}{\pi}}\displaystyle\int_0^a q(X)\frac{\mathrm{d}X}{\sqrt{a-X}} \end{array}\right. \tag{12}$$

and from there, the macroscopic or effective energy release rate G through Irwin's formula:

$$G = \frac{1-\nu^2}{E}\left(K_I^2 + \frac{1}{1-\nu}K_{III}^2\right). \tag{13}$$

Let us introduce the following dimensionless quantities:

$$\beta = \frac{K_{III}^{(0)}}{K_I^{(0)}}, X^* = \frac{X}{a}, p^* = \frac{p\sqrt{2\pi a}}{K_I^{(0)}}, q^* = \frac{q\sqrt{2\pi a}}{K_I^{(0)}}, \mathbf{\Sigma}^* = \frac{\mathbf{\Sigma}\sqrt{2\pi a}}{K_I^{(0)}}, {K^*}_p = \frac{K_p}{K_I^{(0)}}, G^* = \frac{G}{G^{(0)}}, \tag{14}$$

where

$$G^{(0)} = \frac{1-\nu^2}{E}\left({K_I^{(0)}}^2 + \frac{1}{1-\nu}{K_{III}^{(0)}}^2\right). \tag{15}$$

The preceding equations become:

$${K^*}_I = \frac{1}{\pi}\int_0^1 p^*(X^*)\frac{\mathrm{d}X^*}{\sqrt{1-X^*}}, \quad {K^*}_{III} = \frac{1}{\pi}\int_0^1 q^*(X^*)\frac{\mathrm{d}X^*}{\sqrt{1-X^*}}, \quad G^* = \frac{({K^*}_I)^2 + \frac{1}{1-\nu}({K^*}_{III})^2}{1+\frac{\beta^2}{1-\nu}}. \tag{16}$$

In practice, Eqs. 10 and 11 can be solved using the numerical procedure described in Leblond et al. (2015) to obtain $p(X)$ and $q(X)$ for given values of Poisson's ratio ν, the parameters of the facet geometry c/d, α, η, and the mode mixity β. From there, thanks to Eq. 8, the stress tensor $\mathbf{\Sigma}(X)$ along the CZ in the external problem may be obtained, and therefore also the remote stresses in the internal problem through the relations

$$\sigma_1^\infty = \sigma_{11}^\infty = \Sigma_{ZZ}(X), \quad \sigma_2^\infty = \sigma_{22}^\infty = \Sigma_{YY}(X), \quad \sigma_3^\infty = \sigma_{12}^\infty = -\Sigma_{YZ}(X). \tag{17}$$

(These relations result from the different orientations of the frames (x_1, x_2, x_3) and (X, Y, Z) of the internal and external problems respectively, see Fig. 3).

3.2. Examples

Eqs. 10, and 11 rewritten in dimensionless form using Eq. 14, are solved using the same procedure as in Leblond et al. (2015), using the values of the functions $\mathcal{F}_\lambda^p$ presented in Fig. 5 and spline interpolation of the tractions p and q between the available discrete values. We use 51 nodes (where discrete values of p and q are defined) and 50 collocation points (where the integral equations are written) along the segment $X^* \in [0, 1]$, which is checked to be sufficient for mesh independence. The mesh is refined near the points $X^* = 0$ (origin of the CZ) and $X^* = 1$ (tip of the CZ) since large variations of $p^*(X^*)$ and $q^*(X^*)$ may be expected there.

The dependence of p^* and q^* with the parameter η characterizing the coalescence rate (see Eq. 5 for its definition) is given in Fig. 6, where $\nu = 0.4$, $\beta = 0.3$, $c/d = 1.2$, $\alpha = 27°$, corresponding to the experiments of Fig. 1, and the value of η is varied between 0.01 and 0.5. As expected, these tractions decrease to zero when η decreases to zero, since the facets then vanish and their effect disappears. Also noticeable is the divergence of the functions near $X^* = 0$. (This divergence may be demonstrated analytically but the heavy and rather useless proof is omitted for lightness).

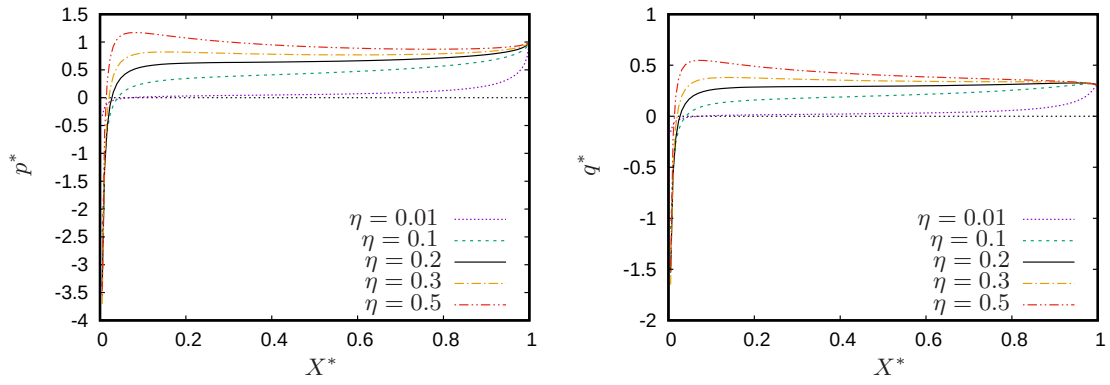

Figure 6: The additional tractions $p^*(X^*)$ and shear forces $q^*(X^*)$ acting on the CZ due to its partial opening ($\nu = 0.4$, $K^{(0)}_{III}/K^{(0)}_{I} = 0.3$, $c/d = 1.2$, $\alpha = 27°$ and η is varied around $\eta = 0.2$ corresponding to the experiments of Fig. 1).

The evolution of the normalized energy-release-rate $G^* = G/G^{(0)}$ with η is given in Fig. 7; also given in the same figure is the dependence of G^* versus c/d for $\eta = 0.2$, using either the approximate solution (Eqs. 4) for the functions $\mathcal{F}^p_\lambda$, or those obtained in the XFEM calculations. Several remarks are in order:

- In the experiments of Fig. 1, $c/d \sim 1.2$ and $\eta \sim 0.2$. In Fig. 7, the plots on the left show that for $c/d \geq 0.8$, the approximate solution of Leblond and Frelat (2014) becomes inaccurate and use of the numerical solution including possible overlapping of the facets becomes mandatory. On the right, the dependence of G^* versus η for $c/d \sim 1.2$ obtained using the XFEM solution is given for several values of ν, evidencing an almost complete lack of dependence of G^* upon ν.

- $G/G^{(0)} < 1$ in all cases which means that the body releases less elastic energy through propagation of tilted facets than through propagation of a planar crack. This is because in the case of tilted facets, the release of elastic energy is hindered by the permanence of unbroken ligaments between them.

- The ratio $G/G^{(0)}$ decreases to zero when the ratio $\eta \equiv d/a$ goes to zero, the ratio c/d remaining fixed, or when c/d goes to zero, the parameter η being fixed. This is because an increase of facet length a or a decrease of facet width c for fixed geometrical period d, induces a decrease of the displacement discontinuity across the cohesive zone, that is a closure of this zone unfavourable to the release of

elastic energy.

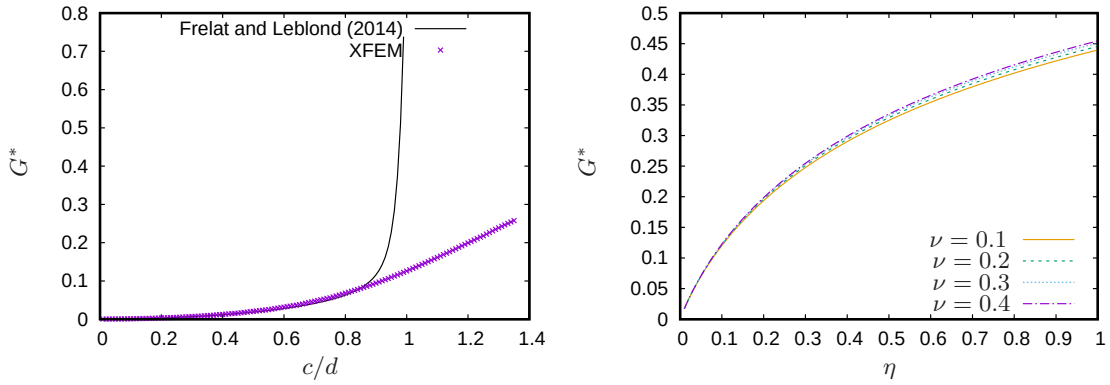

Figure 7: Left: Evolution of $G/G^{(0)}$ with c/d for $\eta = 0.2$. For $c/d > 0.8$, the approximate solution of Leblond and Frelat (2014) becomes inaccurate. Right: Evolution of $G/G^{(0)}$ with η using the XFEM solution ($c/d = 1.2$). Values are independent of ν. In both figures, $K_{III}^{(0)}/K_I^{(0)} = 0.3$, $\alpha = 27°$.

4. Determination of the rotation angle α

We shall now discuss how the cohesive zone model can be used to predict the rotation angle α.

4.1. Criteria

Concerning the direction of propagation, two criteria are investigated: the Principle of Local Symmetry (PLS) stating that the propagation occurs in the direction corresponding to zero mode II (Goldstein and Salganik, 1974); (ii) energy minimization or *Griffith's* principle, consisting in minimizing the total energy $\mathcal{W}_{tot}$ defined as the sum of elastic and fracture energies (Griffith, 1920; Francfort and Marigo, 1998).

4.1.1. Criterion based on the Principle of Local Symmetry (PLS)

A first possibility is to focus on the lateral propagation of the facets. As written in Leblond and Frelat (2014): "The heuristic postulate made is that the 2D SIF k_{II} is zero along the lateral sides of the facets (...) if k_{II} were not zero, lateral propagation of these facets would induce them to deviate out of their plane so that the tilt angle would not be stationary". Using Eq. 3 and equating k_{II} to zero, an implicit equation on α is obtained:

$$\sigma_1^\infty \mathcal{F}_1^{II}\left(\frac{c}{d},\alpha\right) + \sigma_2^\infty \mathcal{F}_2^{II}\left(\frac{c}{d},\alpha\right) + \sigma_3^\infty \mathcal{F}_1^{II}\left(\frac{c}{d},\alpha\right) = 0. \tag{18}$$

Depending on whether this equation is solved for fixed c/d or fixed ℓ/d using the relation $\ell = c/\cos\alpha$ (ℓ is the half-width of a facet as shown in Fig. 3(a)), different values of α are obtained. We take the option to fix ℓ/d which seems more pertinent from a physical point of view, since ℓ is determined by the lateral propagation of the facets, whereas c combines the half-width of the facet ℓ and its orientation α.

4.1.2. Criterion based on energy minimisation (Wmin)

Another possibility, focussing on the output of the facet propagation in the $X-$direction, is based on the minimization of $\mathcal{W}_{tot}$. Strictly speaking, the minimization should be done step by step and look, at each load increment, for the crack path which minimizes $\mathcal{W}_{tot}$. This task can only be done numerically and involves some cumbersome simulations (Pons and Karma, 2010; Chen et al., 2015; Henry, 2016; Pham and Ravi-Chandar, 2017; Lo et al., 2019; Mesgarnejad et al., 2019) based on approximate ways of regularizing the problem (Bourdin et al., 2000; Hakim and Karma, 2009; Miehe et al., 2010). Here, we simplify the problem by assuming that during its evolution, the crack has 'time' to select, among several states, that corresponding to a minimum, with respect to the angle α, of the total energy $\mathcal{W}_{tot}^{\mathrm{2D}}$ of the 2D internal problem (illustrated in Fig. 3(a)). Such an argument has been used with success in other similar situations, for instance by Gauthier et al. (2010); Maurini et al. (2013) for star shape configurations obtained in experiments of directional drying of colloidal suspensions. The total energy $\mathcal{W}_{tot}^{\mathrm{2D}}$ per period splits into two terms:

- the fracture energy, which is simply $2G_c\ell$,
- the elastic energy, which is equal to that without any crack (W_0) reduced by the energy $2\int_0^\ell g(\ell')\mathrm{d}\ell'$ released by propagation of the cracks, where g is the energy-release-rate in the internal problem. This energy-release-rate is equal to $\frac{4(1-\nu^2)d^2}{E}\sigma_\lambda^\infty\sigma_\mu^\infty\mathcal{A}_{\lambda\mu}\left(\frac{\ell}{d}\cos\alpha,\alpha\right)$ (use Eqs. 5 and 17 of Leblond et al., 2015).

Thus one must look for the minimum value with respect to α of the quantity:

$$\mathcal{W}_{tot} = W_0 - \frac{4(1-\nu^2)d^2}{E}\sigma_\lambda^\infty\sigma_\mu^\infty\mathcal{A}_{\lambda\mu}\left(\frac{\ell}{d}\cos\alpha,\alpha\right) + 2G_c\ell. \tag{19}$$

Again it seems physically more pertinent to perform this minimization for a fixed value of ℓ/d rather than c/d. (Anyway one can check that there is no minimum for a constant c/d).

4.2. Determination of the remote loading

Eqs. 18 and 19 may be solved using the remote loading $\boldsymbol{\sigma}^\infty$ of the internal problem as an input. This gives α as a function of $\boldsymbol{\sigma}^\infty$. This remote loading depends on the specimen and loading considered. Leblond and Frelat (2014) considered several special cases in which $\boldsymbol{\sigma}^\infty$ was related only to the mode mixity β. Here we shall consider, in coherence with our experimental setup (see Fig. 1), that the initial crack is loaded by a uniform remote stress field $\boldsymbol{\sigma}^\infty = \sigma^\infty\mathbf{j}\otimes\mathbf{j}$ with $\mathbf{j} = \cos\Gamma_0\mathbf{e}_X + \sin\Gamma_0\mathbf{e}_Z = \cos\Gamma_0\mathbf{e}_2 - \sin\Gamma_0\mathbf{e}_1$, so that $\sigma_1^\infty = \sigma^\infty\sin^2\Gamma_0$, $\sigma_2^\infty = \sigma^\infty\cos^2\Gamma_0$, $\sigma_3^\infty = -\sigma^\infty\sin\Gamma_0\cos\Gamma_0$. The angle Γ_0 here denotes the inclination of the crack in this stress field.

The CZ model provides another way to obtain $\boldsymbol{\sigma}^\infty$ from knowledge of the mode mixity β using Eqs. 17 and 8. The dependence on X of the stresses Σ_{ij} given by Eqs. 8 is relatively weak far from the points $X^* = 0$ and $X^* = 1$ (where the solution is invalid anyway, see Leblond et al. (2015)). Accordingly we

choose to consider the values of these stresses at the middle of the CZ, that is $\sigma_1^\infty = \Sigma_{ZZ}(X = a/2)$, $\sigma_2^\infty = \Sigma_{YY}(X = a/2)$, $\sigma_3^\infty = -\Sigma_{YZ}(X = a/2)$. Since p and q depend on c/d and α, equations Eqs. 18-19 must be solved accounting for the fact that the σ_λ^∞, similarly to the $\Sigma_{pq}(X = a/2)$, themselves depend on ℓ/d and the unknown α. The output consists of the value of α, obtained as a function of ℓ/d for given values of η, β and ν.

4.3. Some results

4.3.1. Asymptotic versus XFEM, and PLS versus Wmin

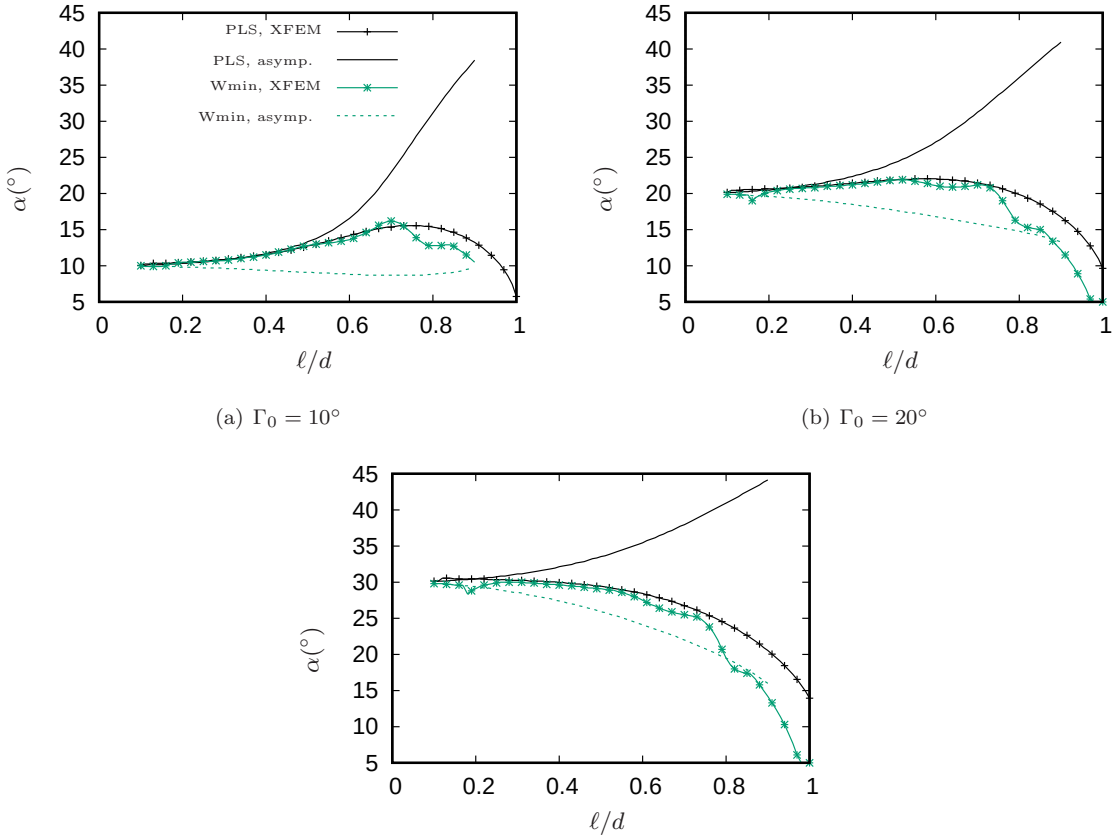

(a) $\Gamma_0 = 10°$

(b) $\Gamma_0 = 20°$

(c) $\Gamma_0 = 30°$

Figure 8: Rotation α of the facets for a crack loaded initially by the stress $\boldsymbol{\sigma}^\infty = \sigma^\infty \mathbf{j} \otimes \mathbf{j}$ with $\mathbf{j} = \cos\Gamma_0 \mathbf{e}_2 - \sin\Gamma_0 \mathbf{e}_1$. 'PLS' denotes the predictions obtained by imposing $k_{II} = 0$ at the lateral tips, 'Wmin' by minimizing the energy. Solid lines are obtained using the asymptotic values (Eqs. 4) of the functions $\mathcal{F}_\lambda^p$, points using the numerical values obtained by XFEM. The results deriving from asymptotic values are observed to quickly become inaccurate, especially for the Wmin criterion.

As discussed above, we consider that the initial crack is loaded by a uniform remote stress field $\boldsymbol{\sigma}^\infty = \sigma^\infty \mathbf{j} \otimes \mathbf{j}$. Figures 8 provides the values of α as a function of ℓ/d for several values of Γ_0, obtained from

Eqs. 18 and 19. Note that since $\mathcal{F}^p_\lambda$ and thus $\mathcal{A}_{\lambda\mu}$ (Eqn. 7) are independent of ν (§2.1), it is also the case for these plots. The results are shown using either the approximate values (Eqs. 4) of the functions $\mathcal{F}^p_\lambda$ or those obtained by XFEM. Several observations can be made:

- *Numerical artefacts in the Wmin criterion.* A small perturbation around $\ell/d = 0.15$ in the values of α can be noticed. It is a numerical artefact due to the transition from use of the asymptotic values of the functions $\mathcal{F}^p_\lambda$ (formula 4) to the numerical values (Fig. 5). It shows the sensitivity of the minimization with respect to the values of $\mathcal{F}^p_\lambda$: the perturbation in α around $\ell/d = 0.15$ is large although the approximate and numerical values of the functions $\mathcal{F}^p_\lambda$ are close (see Fig. 5). Also, the fluctuations appearing for $\ell/d > 0.5$ are probably linked to increasing numerical errors with higher values of ℓ/d. Besides, we have also noticed that using linear instead of spline interpolation for the functions $\mathcal{F}^p_\lambda$, we get unphysical oscillating solutions $\alpha(\ell/d)$. Accurate predictions in the region $\ell/d > 0.5$ would require additional numerical efforts.

- *Accuracy of the asymptotic formulas.* For small values of ℓ/d, it can be checked that α derived from the XFEM values of $\mathcal{F}^p_\lambda$ are in agreement with those obtained using their asymptotic formulas. The discrepancy for larger values is due to the inaccuracy of the asymptotic values which are derived in the limit $\ell/d \to 0$.

- *Equivalence of the PLS and Wmin criteria.* In the limit $\ell/d \to 0$ both criteria give the same result. This can be explained by the fact that then, each facet behaves like an isolated crack in an infinite 2D body, inclined by an angle α and loaded remotely by $\boldsymbol{\sigma}^\infty$. The lateral SIFs k_I, k_{II} are proportional to N and T respectively, the far normal and tangential stresses to the facet, and the term depending on α in $\mathcal{W}_{tot}$ is negatively proportional to $N^2 + T^2$. Thus the minimum of $\mathcal{W}_{tot}$ corresponds to the maximum of $N^2 + T^2$, which is achieved for $T = 0$ by Mohr's construction. This implies that the Wmin criterion is equivalent to the PLS in this limit.

  For larger values, the predictions of both criteria can be noticed to be similar, although the criteria have no reason to coincide under such conditions.

- *Facet shape.* As long as the facet width remains small enough, the facets behave independently and the variation of α with ℓ/d itself remains small. This explains why their shape observed experimentally is straight near the middle (Fig. 1 and 4). Their orientation is observed to remain close to the shear free direction $\alpha = \Gamma_0$.

  The angle α slightly increases or decreases when ℓ/d increases, depending on the value of Γ_0. This variation may be seen as an early sign of a repulsion or attraction of the en-passant S-shape (Schwaab et al., 2018).

Finally, as awaited since Eqs. 4 are valid only for small values of α or c/d, the evolution of α with ℓ/d is different according to whether the approximate or numerical values of the functions $\mathcal{F}_\lambda^p$ are used. The error made using asymptotic values instead of the more accurate numerical one is huge specially for Wmin where a notable difference is observed as soon as $\ell/d > 0.2$. This justifies the numerical effort made to obtain the values of the functions $\mathcal{F}_\lambda^p$ for larger values. In the sequel, all results will be presented using these numerical values.

4.3.2. Comparison with the experiments

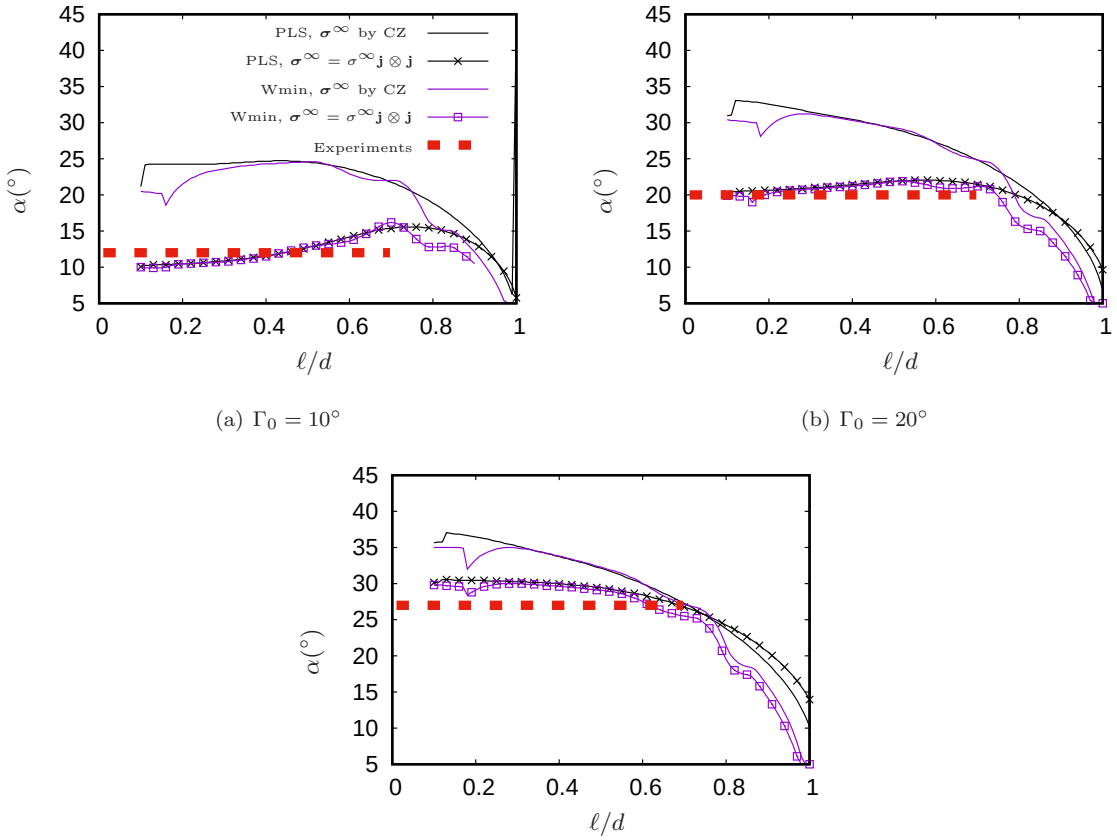

(a) $\Gamma_0 = 10°$

(b) $\Gamma_0 = 20°$

(c) $\Gamma_0 = 30°$

Figure 9: α as a function of ℓ/d for several values of Γ_0. Solid lines are obtained using the remote loading from the CZ model using $\beta = \frac{1}{2}\tan\Gamma_0$, $\nu = 0.4$, $\eta = 0.2$. Solid lines with points correspond to $\sigma_1^\infty = \sigma^\infty \sin^2\Gamma_0$, $\sigma_2^\infty = \sigma^\infty \cos^2\Gamma_0$, $\sigma_3^\infty = -\sigma^\infty \sin\Gamma_0\cos\Gamma_0$ like in Fig. 8. The horizontal red dotted line corresponds to a rough estimation of the inclination of the facets in their straight portion. The line is stopped at $\ell/d = 0.7$ since above the facets can be observed to bend significantly (see Fig. 4).

In Fig. 9, the predictions from the PLS and Wmin criteria are given, using the remote loading defined by $\boldsymbol{\sigma}^\infty = \sigma^\infty \mathbf{j}\otimes\mathbf{j}$, with $\mathbf{j} = \cos\Gamma_0\mathbf{e}_2 - \sin\Gamma_0\mathbf{e}_1$ like in Fig. 8, or that obtained from the CZ model using

$\beta = \frac{1}{2}\tan\Gamma_0$, $\nu = 0.4$, $\eta = 0.2$ corresponding to our 4PB experiments of section 1. The corresponding experimental values are also plotted in this figure. It is the slope of the facets in their straight section (where the angle α is thus constant). The lines are stopped at the point ℓ/d where the facets start to bend. The measures are made directly on Fig. 1 and 4, hence are rough estimations.

Using $\boldsymbol{\sigma}^\infty = \sigma^\infty \mathbf{j} \otimes \mathbf{j}$, a good agreement is found in the range $\ell/d \in [0.2; 0.6]$: the predicted values are closed to the average experimental one in the whole range and their variation with ℓ/d is weak in accordance with the straightness of the crack in this zone (Fig. 4). Precise modulations of α with ℓ/d are difficult to detect experimentally. And anyway, such variations can not be caught by our approach which considers the segments as invariant in the propagation direction.

Using $\boldsymbol{\sigma}^\infty$ derived from the CZ model fails to predict the values of α obtained in the experiments. One reason may be that the CZ model assumes an infinite body and can thus only be used to obtain the remote loading if the effect of the lateral boundary conditions can be neglected. This may not be the case in these experiments. The better agreement with $\boldsymbol{\sigma}^\infty = \sigma^\infty \mathbf{j} \otimes \mathbf{j}$ can be rationalized by the fact that in the 4 PB experiments the far field is indeed of this form (see Fig. 1), especially for slight inclinations of the crack (small values of Γ_0). Another source of discrepancies may come from the sensitivity of the results to Poisson' ratio, as will be highlighted below.

4.3.3. Parametric study

The similarity between the results obtained with the PLS and Wmin criteria, already noted in Fig. 8, is also observed when the remote stress field is deduced from the CZ model. Hence, for the parametric study of the dependence of α upon η, ν and β, we plot only, as a representative case, the results obtained with the PLS criterion. In Fig. 10, the parameters are varied around the values $\eta = 0.2$, $\nu = 0.4$, $\beta = 0.2$, corresponding to the experiment of Fig. 1. Several points are noteworthy:

- the results are nearly independent of η meaning that the dependence of the stresses $\sigma_{11}^\infty = \Sigma_{ZZ}(X = a/2)$, $\sigma_{22}^\infty = \Sigma_{YY}(X = a/2)$, $\sigma_{12}^\infty = -\Sigma_{YZ}(X = a/2)$ with η cancels out in Eq. 18;
- as expected, α increases with the mode mixity ratio β;
- the results are highly sensitive to the value of Poisson's ratio ν, to the point that taking $\nu = 0.3$ instead of $\nu = 0.4$ permits to retrieve the experimental value of α. This means that the study of α is a difficult issue, in which the dependence upon ν has to be considered with care.

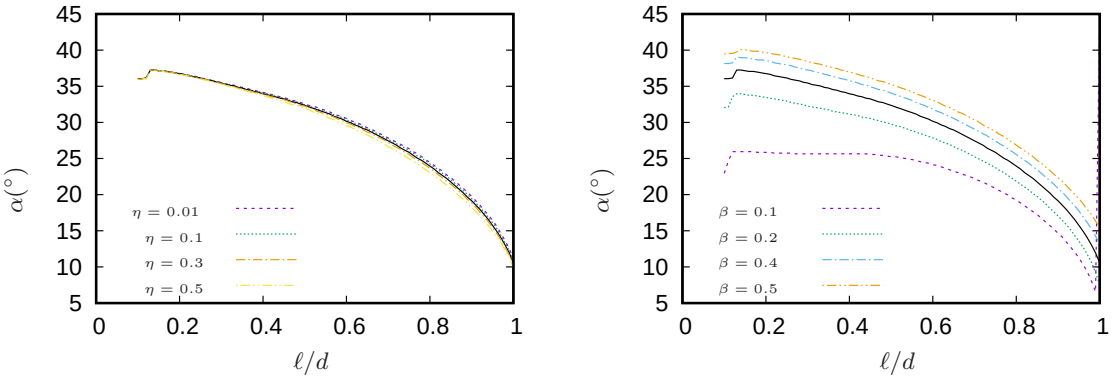

(a) $\beta = 0.3$, $\nu = 0.4$

(b) $\eta = 0.2$, $\nu = 0.4$

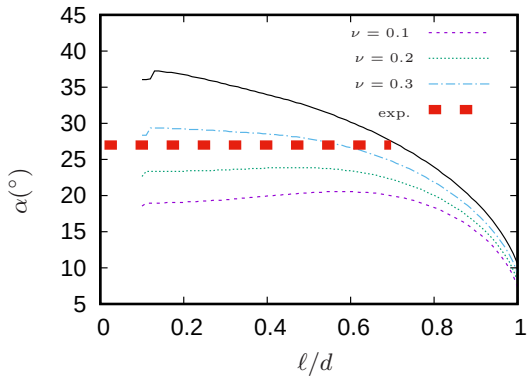

(c) $\eta = 0.2$, $\beta = 0.3$

Figure 10: Dependence of $\alpha(\ell/d)$ upon η, β and ν. The PLS criterion is used with the remote loading from the CZ model. The black solid line corresponds to $\eta = 0.2$, $\beta = 0.3$, $\nu = 0.4$ in all the graphs. The experimental red line is the same than in Fig. 9c.

5. Toughening due to the presence of the facets

5.1. In fatigue

Assume that the propagation of the tips of the facets is ruled by Paris's law:

$$\frac{\mathrm{d}a}{\mathrm{d}N} = C\left(\frac{E}{1-\nu^2}\Delta G\right)^{n/2} \tag{20}$$

where $\frac{\mathrm{d}a}{\mathrm{d}N}$ denotes the crack advance per cycle, ΔG the amplitude of the variation of the energy-release-rate during one cycle. Thanks to Irwin's formula (Eq. 13), this formula reduces to $\frac{\mathrm{d}a(s)}{\mathrm{d}N} = C\left(\Delta K_I(s)\right)^n$ in pure mode I so that the constants C and n are the classical Paris exponents, which are known for a wide range of materials (Fleck et al., 1994).

The energy-release-rate G at the tip of the CZ can be obtained using Eqs. 13 and 12. The result reads, using the notations of Eqs. 15 and 16:

$$\frac{\mathrm{d}a}{\mathrm{d}N} = C_{\mathrm{eff}}\left(\frac{E}{1-\nu^2}\Delta G^{(0)}\right)^{n/2} \tag{21}$$

where the effective Paris' coefficient C_{eff} can be determined by:

$$\left(\frac{C_{\mathrm{eff}}}{C}\right)^{2/n} = G^*. \tag{22}$$

This permits to extend Paris's classical law in mode I to mixed-mode situations without introducing additional material constants. In this view the influence of mode mixity on crack propagation arises only from its effect on the facet geometry.

5.2. In brittle fracture

Assume now that crack propagation becomes possible only once Griffith's threshold is reached:

$$G = G_c \tag{23}$$

where $G_c = \frac{1-\nu^2}{E}K_c^2$, G_c and K_c denoting the classical fracture energy and toughness respectively. These quantitites are classical material constants which are known for a wide range of materials (Ashby, 1989).

The loading $\mathcal{C}^0$ needed for coplanar propagation of the crack is given by $G^{(0)} = G_c$, and the effective energy-release-rate for the same loading in the presence of facets is $G^*G^{(0)}$. Denote $\lambda\mathcal{C}^0$ the loading needed to propagate the facets tips. For this loading, the effective energy release rate is $G = \lambda^2 G^* G^{(0)}$ (use the linearity of K_p with λ and Irwin's formula (Eq. 13)). Over a period of dimension $2d$, the energy released per unit distance of propagation is $2dG = 2d\lambda^2 G^* G^{(0)}$, and this energy must balance a fracture energy of $2\ell G_c$. It follows that

$$\lambda = \sqrt{\frac{\ell}{d}\frac{1}{G^*}} \tag{24}$$

This factor λ depends, like G^* defined in Eqs. 14 and 16, on the facet geometry (α, ℓ/d, η), Poisson's ratio ν and the mixity factor β. Since $G^* \leq 1$ (Fig. 7), while $\frac{\ell}{d}$ is generally observed to be close to or greater than 1, λ is larger than 1. This factor thus appears as a *toughening factor* for fracture under mixed mode I+III loading.

5.3. Some results

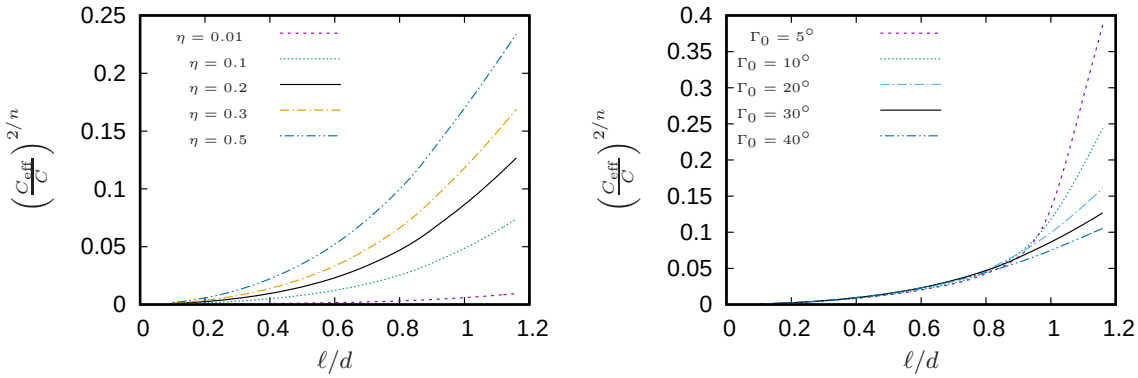

(a) $\Gamma_0 = 30°$ (b) $\eta = 0.2$

Figure 11: Dependence of the effective Paris rate C_{eff} with η and Γ_0 (independence with ν is verified through G^* evidenced in Fig. 7). In all the figures, $\beta = \frac{1}{2}\tan\Gamma_0$ and $\alpha = \Gamma_0$.

In Fig. 11, the effective Paris propagation rate C_{eff} is given in the form of the quantity $\left(\frac{C_{\text{eff}}}{C}\right)^{2/n} = G^*$, independent of Paris' coefficients C and n, as a function of ℓ/d for different values of η and Γ_0; Γ_0 here refers to the experiments described in section 1 for which the values $\beta = \frac{1}{2}\tan\Gamma_0$ and $\alpha = \Gamma_0$ can be considered as good approximations. These plots are almost independent of Poisson' ratio ν (see Fig. 7). One notices that:

- $C_{\text{eff}} < C$, which means that the facets lower the propagation rate at fixed loading amplitude. In other words, the facets enhance the fracture resistance or have a *toughening* effect on fatigue propagation. This effect is due to the existence of ligaments between the facets which hinder their opening.
- C_{eff}/C, which characterizes the propagation rate $\frac{\mathrm{d}a}{\mathrm{d}N}$ at fixed $\Delta G^{(0)}$, decreases to zero together with the facet width ℓ for a given wavelength d and coalescence rate η. This is linked to the fact that the opening of the facets decreases with the facet width ℓ (for fixed loading).
- At fixed Γ_0 and ℓ/d, C_{eff} decreases together with the coalescence rate η. Like before, this is because the opening of the facets is more difficult for smaller values of η.

- The influence of Γ_0 on C_{eff} is weak as long as $\ell/d < 0.8$, that is when the interactions between the facets remain low. This can be linked to the fact that with $\alpha = \Gamma_0$, the facet orientation relative to the remote loading is the same for all values of Γ_0 so that the effective loading at the facet tip is nearly the same. When $\ell/d > 0.8$, interactions between facets start to have an impact which lowers the propagation rate when Γ_0 increases.

- Enhanced fracture resistance has been observed by Eberlein et al. (2017) in agreement with our model. Quantitative comparison with experiments necessitates however in-situ observations of crack propagation to get an estimate of ℓ/d. Final crack profiles such as those measured in Cambonie and Lazarus (2014) or Eberlein et al. (2017) are not sufficient since the ligaments are then broken, erasing any trace of their former shape.

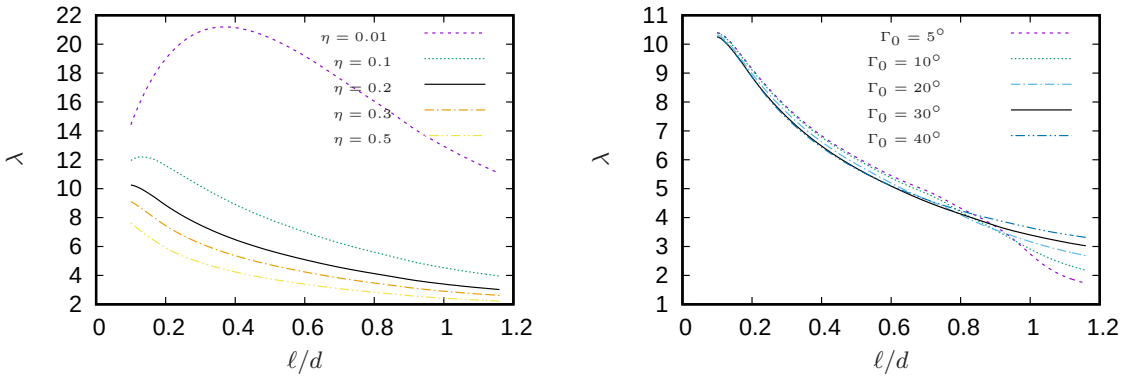

(a) $\Gamma_0 = 30°$ (b) $\eta = 0.2$

Figure 12: Dependence of the effective critical loading for fracture λ upon ℓ/d for several values of η and Γ_0 (independence with respect to ν is verified through G^*, see Fig. 7). In all the figures, $\beta = \frac{1}{2}\tan\Gamma_0$ and $\alpha = \Gamma_0$.

While Fig. 11 concerns fatigue propagation, Fig. 12 relates to brittle fracture and gives the factor λ as a function of ℓ/d for the same values of β and α. One can draw similar conclusions:

- The presence of facets and the existence of unbroken ligaments enhance the fracture threshold yielding $\lambda > 1$.

- As the opening of the facets decreases at fixed loading when the facet width decreases, one gets for a given value of Γ_0, an increase of λ when η decreases at fixed ℓ/d, or when ℓ/d decreases at fixed η.

- The influence of Γ_0 on λ becomes significant only when $\ell/d > 0.8$, that is when the interactions between the facets are stronger.

- Quantitative comparison with experiments necessitates in-situ observations of crack propagation to get an estimate of ℓ/d. This requires quasistatic propagation, that is a setup allowing stable propagation of the crack, which cannot be achieved straightforwardly using the 4PB setup of section 1.

6. Perspectives

Let us draw some perspectives by scrolling back the story from the end. We have seen that the above method permits to quantify the toughening effect by providing C_{eff} and λ, knowing the facet geometry though the constants α, c/d and η and the classical fracture constants G_c, n and C. To be fully efficient and avoid the introduction of additional material constants, the facet geometry must be determined from knowledge of the fracture constants. The determination of α has been discussed in §4 and deserves further studies. The determination of η remains an unresolved issue but fortunately, it is less crucial since C_{eff} and λ depend weakly on this parameter (at least in the limit of our model, that assumes $\eta \ll 1$).

The determination of the c/d relies on consideration of propagation of the lateral tips under the same classical rules as the front tip. That is to say, $\frac{\mathrm{d}c}{\mathrm{d}N} = C\left(\frac{E}{1-\nu^2}\Delta g\right)^{n/2}$ in fatigue and $g = G_c$ for brittle fracture, where g is the energy-release-rate at the lateral tips. The value of g can be obtained from the solution of the internal problem by accounting for Eq. 3 in Eq. 13:

$$g = 2d\,\frac{1-\nu^2}{E}\left[\mathcal{F}_\lambda^I\left(\frac{c}{d},\alpha\right)^2\sigma_\lambda^{\infty 2} + \mathcal{F}_\lambda^{II}\left(\frac{c}{d},\alpha\right)^2\sigma_\lambda^{\infty 2}\right] \tag{25}$$

However the use of this formula is legitimate only if: (i) the lateral extension of the facets is independent of the propagation in the $X-$direction (see Fig. 2) so that the 2D propagations in the internal and external problems are uncoupled; (ii) facets remain straight as they propagate, without any en-passant S-shape. If these hypotheses are not satisfied, numerical simulations (Chen et al., 2015; Henry, 2016; Pham and Ravi-Chandar, 2017; Lo et al., 2019) may be used.

7. Conclusion

Segmentation of the crack front frequently occurs during the propagation of a mode III loaded crack. The unbroken ligaments between the segments/facets by hindering the crack opening, reduce the effective load of the crack tips hence induce an apparent toughening. Using a multiscale cohesive zone model, we achieved to quantify this effect by providing two toughening factors C_{eff} and λ, in fatigue and brittle fracture respectively, as a function of the facet geometry. The model involves some functions $\mathcal{F}_\lambda^p$ related to an array of tilted parallel cracks loaded remotely. Herein, the corresponding elasticity problem has been solved using XFEM calculations, extending previous results (Leblond and Frelat, 2014) to overlapping facets and larger tilt angles, in order to deal with more realistic cases.

This approach derived in the framework of linear elastic fracture mechanics, is valid at any length scales above the size of the material heterogeneities and of the process zone. It thus covers a wide range of observations going basically from the millimeter to any larger scale provided that (i) no ligaments have formed between the facets, (ii) the bending of the facets can be neglected, (iii) the facets are slender enough to separate the initial 3D problem using asymptotic expansion into two 2D problems: one at the microscale, the other at the macroscale.

This approach deserves extensive comparison with experiments specifically designed for this purpose. This will be the goal of a companion paper on the 4PB experiments described in section 1.

Acknowledgements

VL and TC acknowledge the support of ANR GeoSmec (ANR-12-BS06-0016).

References

Ashby, M., 1989. Overview no. 80: On the engineering properties of materials. Acta Metallurgica 37 (5), 1273 – 1293.

Bonniot, T., Doquet, V., Mai, S. H., 2018. Mixed mode II and III fatigue crack growth in a rail steel. International journal of fatigue.

Bourdin, B., Francfort, G. A., Marigo, J. J., 2000. Numerical experiments in revisited brittle fracture. Journal of the Mechanics and Physics of Solids 48 (4), 797–826.

Cambonie, T., Klinger, Y., Lazarus, V., 2019. Similarities between mode III crack growth patterns and strike-slip faults. Philosophical Transactions of the Royal Society of London A: Mathematical, Physical and Engineering Sciences 377 (2136).

Cambonie, T., Lazarus, V., 2014. Quantification of the crack fragmentation resulting from mode I+III loading. Procedia Materials Science 3, 1816–1821.

CEA (French Atomic Commission), 2017. Cast3M: Finite element program. `www-cast3m.cea.fr`.

Chen, C.-H., Cambonie, T., Lazarus, V., Nicoli, M., Pons, A. J., Karma, A., 2015. Crack Front Segmentation and Facet Coarsening in Mixed-Mode Fracture. Physical Review Letters 115 (26), 265503.

Cooke, M. L., Pollard, D. D., 1996. Fracture propagation paths under mixed mode loading within rectangular blocks of polymethyl methacrylate. Journal of Geophysical Research 101 (B2), 3387–3400.

Eberlein, A., Richard, H., Kullmer, G., 2017. Facet formation at the crack front under combined crack opening and anti-plane shear loading. Engineering Fracture Mechanics 174, 21 – 29, special Issue on Multiaxial Fracture 2016.

Erdogan, G., Sih, G. C., 1963. On the crack extension in plates under plane loading and transverse shear. ASME J. Basic Engng 85, 519–527.

Flavien, F., 2012. Fissuration par fatigue en mode mixte I+II+III non proportionnel dans l'acier 316l approche expérimentale et modélisation des effets de la plasticité. Ph.D. thesis, ENS Cachan.

Fleck, N., Kang, K., Ashby, M., 1994. Overview no. 112: The cyclic properties of engineering materials. Acta Metallurgica et Materialia 42 (2), 365 – 381.

Flores, M., Xu, L. R., 2013. An efficient mixed-mode brittle fracture experiment using paper. International Journal of Fracture 183 (2), 267–273.

Francfort, G. A., Marigo, J. J., 1998. Revisiting brittle fracture as an energy minimization problem. Journal of the Mechanics and Physics of Solids 46, 1319–1342.

Gauthier, G., Lazarus, V., Pauchard, L., 2010. Shrinkage star-shaped cracks: Explaining the transition from 90 degrees to 120 degrees. EPL 89, 26002.

Ghelichi, R., Kamrin, K., 2015. Modeling growth paths of interacting crack pairs in elastic media. Soft Matter 11, 7995–8012.

Gibert, Prabel, Gravouil, Jacquemoud, 2019. A 3D automatic mesh refinement X-FEM approach for fatigue crack propagation. Finite Elements in Analysis and Design 157.

Goldstein, R., Osipenko, N., 2012. Successive development of the structure of a fracture near the front of a longitudinal shear crack. Doklady Physics 57, 281–284, 10.1134/S1028335812070087.

Goldstein, R. V., Salganik, R. L., 1974. Brittle fracture of solids with arbitrary cracks. International Journal of Fracture 10, 507–523.

Gravouil, A., Moes, N., Belytschko, T., 2002. Non-planar 3d crack growth by the extended finite element and level sets. II. Level set update. International Journal for Numerical Methods in Engineering 53 (11), 2569–86.

Griffith, A. A., 1920. The phenomena of rupture and flow in solids. Philosophical Transactions of the Royal Society of London 221, 163–198.

Hakim, V., Karma, A., 2009. Laws of crack motion and phase-field models of fracture. Journal of the Mechanics and Physics of Solids 57 (2), 342 – 368.

Henry, H., 2016. Crack front instabilities under mixed mode loading in three dimensions. EPL (Europhysics Letters) 114 (6), 66001.

Hull, D., 1993. Tilting cracks: the evolution of fracture surface topology in brittle solids. International Journal of Fracture 62 (2), 119–138.

Hull, D., 1995. The effect of mixed-mode I/III on crack evolution in brittle solids. International Journal of Fracture 70 (1), 59–79.

Lazarus, V., Buchholz, F.-G., Fulland, M., Wiebesiek, J., 2008. Comparison of predictions by mode II or mode III criteria on crack front twisting in three or four point bending experiments. International Journal of Fracture 153, 141–151.

Lazarus, V., Leblond, J.-B., Mouchrif, S.-E., 2001a. Crack front rotation and segmentation in mixed mode I+III or I+II+III - part I: Calculation of Stress Intensity Factor. Journal of the Mechanics and Physics of Solids 49 (7), 1399–1420.

Lazarus, V., Leblond, J.-B., Mouchrif, S.-E., 2001b. Crack front rotation and segmentation in mixed mode I+III or I+II+III - part II: Comparison with experiments. Journal of the Mechanics and Physics of Solids 49 (7), 1421–1443.

Leblond, J., Karma, A., Lazarus, V., 2011. Theoretical analysis of crack front instability in mode I+III. Journal of the mechanics and physics of Solids 59, 1872–1887.

Leblond, J.-B., Frelat, J., 2014. Development of fracture facets from a crack loaded in mode I+III: solution and application of a model 2D problem. Journal of the Mechanics and Physics of Solids 64, 133–153.

Leblond, J.-B., Karma, A., Ponson, L., Vasudevan, A., 2019. Configurational stability of a crack propagating in a material with mode-dependent fracture energy - part I: Mixed-mode I+III. Journal of the Mechanics and Physics of Solids 126, 187 – 203.

Leblond, J.-B., Lazarus, V., Aug. 2015. On the strong influence of imperfections upon the quick deviation of a mode I+III crack from coplanarity. Journal of Mechanics of Materials and Structures 10 (3), 299–315.

Leblond, J.-B., Lazarus, V., Karma, A., February 2015. Multiscale cohesive zone model for propagation of segmented crack fronts in mode I+III fracture. International Journal of Fracture (Special Invited Article Celebrating IJF at 50) 191 (1), 167–189.

Leblond, J.-B., Torlai, O., 1992. The stress field near the front of an arbitrarily shaped crack in a three-dimensional elastic body. Journal of Elasticity 29 (2), 97–131.

Lin, B., Mear, M., Ravi-Chandar, K., 2010. Criterion for initiation of cracks under mixed-mode I+III loading. International Journal of Fracture 165, 175–188.

Lo, Y.-S., Borden, M. J., Ravi-Chandar, K., Landis, C. M., 2019. A phase-field model for fatigue crack growth. Journal of the

Mechanics and Physics of Solids 132, 103684.

Maurini, C., Bourdin, B., Gauthier, G., Lazarus, V., 2013. Crack patterns obtained by unidirectional drying of a colloidal suspension in a capillary tube: experiments and numerical simulations using a two-dimensional variational approach. International Journal of Fracture 184 (1-2), 75–91.

Melin, S., 1983. Why do cracks avoid each other? International Journal of Fracture 23, 37–45.

Mesgarnejad, A., Imanian, A., Karma, A., 2019. Phase-field models for fatigue crack growth. Theoretical and Applied Fracture Mechanics 103, 102282.

Miehe, C., Hofacker, M., Welschinger, F., 2010. A phase field model for rate-independent crack propagation: Robust algorithmic implementation based on operator splits. Computer Methods in Applied Mechanics and Engineering 199 (45), 2765 – 2778.

Muskhelishvili, N. I., 1953. Some Basic Problems of the Mathematical Theory of Elasticity. Noordhoff, Groningen.

Palaniswamy, K., Knauss, W. G., 1975. Crack extension in brittle solids. Mechanics Today, Pergamon Press 4, 87.

Pham, K. H., Ravi-Chandar, K., 2014. Further examination of the criterion for crack initiation under mixed-mode I+III loading. International Journal of Fracture 189 (2), 121–138.

Pham, K. H., Ravi-Chandar, K., 2016. On the growth of cracks under mixed-mode I + III loading. International Journal of Fracture, 1–30.

Pham, K. H., Ravi-Chandar, K., Aug 2017. The formation and growth of echelon cracks in brittle materials. International Journal of Fracture 206 (2), 229–244.

Pham, K. H., Ravi-Chandar, K., Landis, C. M., May 2017. Experimental validation of a phase-field model for fracture. International Journal of Fracture 205 (1), 83–101.

Pollard, D. D., Segall, P., Delaney, P. T., 1982. Formation and interpretation of dilatant echelon cracks. Geological Society of America Bulletin 93, 1291–1303.

Pons, A. J., Karma, A., 2010. Helical crack-front instability in mixed-mode fracture. Nature 464, 85–89.

Pook, L., 1995. On fatigue crack paths. International Journal of Fatigue 17 (1), 5–13.

Prabel, B., Yuritzinn, T., Charras, T., Simatos, A., 2011. Propagation de fissures tridimensionnelles dans des matériaux inélastiques avec XFEM dans Cast3m. In: 10e colloque national en calcul des structures.

Pulos, G. C., Knauss, W. G., 1998. Nonsteady crack and craze behavior in PMMA under cyclical loading: III. effect of load history on cohesive force distribution on the craze. International Journal of Fracture 93 (1-4), 187–207.

Ronsin, O., Caroli, C., Baumberger, T., Feb. 2014. Crack front échelon instability in mixed mode fracture of a strongly nonlinear elastic solid. EPL (Europhysics Letters) 105 (3), 34001.

Schwaab, M.-E., Biben, T., Santucci, S., Gravouil, A., Vanel, L., Jun 2018. Interacting cracks obey a multiscale attractive to repulsive transition. Phys. Rev. Lett. 120, 255501.

Sommer, E., 1969. Formation of fracture 'lances' in glass. Engineering Fracture Mechanics 1, 539–546.

Wei, Y., Gao, H., Bower, A. F., 2009. Numerical simulations of crack deflection at a twist-misoriented grain boundary between two ideally brittle crystals. Journal of the Mechanics and Physics of Solids 57 (11), 1865 – 1879.

Wu, R., 2006. Some fundamental mechanisms of hydraulic fracturing. Ph.D. thesis, Georgia Institute of Technology.

Appendix A. Computation of periodic cracks distribution using XFEM coupled with hierarchical mesh refinement

Appendix A.1. 2-Dimensional Linear Elastic Fracture Mechanical problem

Like in the paper of Leblond and Frelat (2014), a 2D infinite periodic array of inclined cracks is considered (Fig. 3(a)). The two geometric parameters characterizing the problem are:

- the tilt angle: α,
- the ratio of crack length along x_1 to the period: $\frac{c}{d}$.

Three elementary loadings (σ_1^∞, σ_2^∞ and σ_3^∞) may be considered, and then, thanks to linearity of the problem, the stress intensity factors k_I and k_{II} can be expressed as functions of these three loadings:

$$k_p = \sqrt{2d} \sum_i \mathcal{F}_i^p \left(\alpha, \frac{c}{d}\right) \sigma_i^\infty \tag{A.1}$$

for $p = I, II$ and $i = 1, 2, 3$.

The factor $\sqrt{2d}$ is chosen instead of the factor $\sqrt{2d \tan(\pi c/2d)}$ of Leblond and Frelat (2014) because it is limiting the possible range of c/d to values less than 1.

Appendix A.2. Finite Element computations

Periodicity enables to limit the spatial domain to $x_1 \in [0 - 2d]$ (with the (x_1, x_2)-frame depicted on Fig. 3(a)). Along x_2, the domain is limited at $\pm 10d$, which has been found sufficiently large to be considered as an quasi-infinite boundary.

The aim of finite element computations is to determine accurately the six functions $\mathcal{F}_i^p(\alpha, \frac{c}{d})$. To this end, a parametric study is performed for $\alpha \in [0° - 45°]$ and $\frac{c}{d} \in [0 - 1.4]$. To avoid intersecting cracks, the range of α is limited to $[5° - 45°]$ for $\frac{c}{d} \geq 1$.

A "classical" Finite Element approach for parametric study would be to create a procedure enable to generate a parametric mesh conforming the cracks location for every combination of α and $\frac{c}{d}$. However creating such a procedure is a burden if one wish to verify at the same time:

- a sufficiently rough mesh size away from crack tip to maintain the computational time reasonable,
- a sufficiently fine mesh size at crack tips vicinity to ensure an accurate solution,
- a regular mesh around crack tip enabling an accurate computation of interaction integrals (necessary to determine the stress intensity factors),
- and a symmetric mesh to facilitate the imposition of periodic boundary conditions and the interpretation of results,

for all considered situations.

Conversely, the XFEM combined with a hierarchical mesh refinement is found to be a very easy way to perform the present parametric study at the condition to elaborate the numerical model rigorously. In parallel to the present work, such an approach has been followed to compute mixed-mode crack propagation in Gibert et al. (2019). The procedure describes hereafter has been implemented in Cast3M CEA (French Atomic Commission) (2017) software and tends to prove its efficiency.

1. First a regular mesh composed of quadrilateral elements is generated for the sane structure and a line-mesh defining the cracks location is also created (Fig. 13(a))
2. A hierarchical mesh refinement procedure is performed in order to get a suitable mesh size at the crack tip. Figures 13(b), 13(c) and 13(d) represent three levels of mesh refinement adopted to check convergence of computations. The mesh size vary between $\frac{d}{8}$ to $\frac{d}{64}$ for the first one, between $\frac{d}{20}$ to $\frac{d}{160}$ for the second one, and between $\frac{d}{40}$ to $\frac{d}{640}$ for the finest one. This last mesh is the one used as reference and to plot the curves representing the $\mathcal{F}$-functions.
3. Level sets function $\phi(\underline{x})$ and $\psi(\underline{x})$ are computed at nodes sufficiently close to the crack geometry and define the local frame at the crack tip. This explicit/implicit crack description is presented in Prabel et al. (2011) The XFEM approximation of displacement is adopted to include the presence of cracks:

$$\underline{u}(\underline{x}) = \sum_i N_i(\underline{x})\underline{U}_i + \sum_{i\in I_A} N_i(\underline{x})H(\underline{x})\underline{A}_i + \sum_{i\in I_B}\sum_j N_i(\underline{x})F_j(\underline{x})\underline{B}_{ij} \tag{A.2}$$

   with the enrichment functions $H = \text{sign}(\phi)$, $F_1 = \sqrt{r}\sin(\theta/2)$, $F_2 = \sqrt{r}\sin(\theta/2)\sin(\theta)$, $F_3 = \sqrt{r}\cos(\theta/2)$ and $F_4 = \sqrt{r}\cos(\theta/2)\sin(\theta)$, and where I is the set of all nodes, and I_A and I_B denotes two well-chosen sets of nodes to be enriched.
4. Stiffness matrix, conformity relations and boundary conditions are created.
   As the enrichment lays only in the finest zone, conformity relations only concern the "standard" degree-of-freedom of hanging nodes:

$$\underline{U}_{\text{Hanging}} = \frac{1}{2}\underline{U}_1 + \frac{1}{2}\underline{U}_2 \tag{A.3}$$

   where the hanging node is at the center of the segment constituted of nodes 1 and 2.
   Periodicity of the solution have to be written carefully because of XFEM enrichment. Defining as I_0 and I_{2d} the set of nodes lying respectively at $x_1 = 0$ and $x_1 = 2d$, it can be shown that the kinematic relations involving only U and A degrees-of-freedom to be imposed for this particular problem are:

$$\underline{u}(x_1 = 0, x_2) - \underline{u}(x_1 = d, x_2) = -\underline{\underline{\epsilon}}^{\infty} \cdot 2d\underline{e}_1 \tag{A.4a}$$

$$\Leftrightarrow \begin{cases} \underline{U}_i - \underline{U}_j = -\underline{\underline{\epsilon}}^{\infty} \cdot 2d\underline{e}_1 & \text{for } i \in (I \setminus I_A) \cap I_0 \\ & \text{and } j \in (I \setminus I_A) \cap I_{2d} \\ \underline{U}_i + \text{sign}(\phi_i)\underline{A}_i - \underline{U}_j - \text{sign}(\phi_j)\underline{A}_j = -\underline{\underline{\epsilon}}^{\infty} \cdot 2d\underline{e}_1 & \text{for } i \in I_A \cap (I_0 \setminus \{\underline{x}_i : x_{i\,2} = 0\}) \\ & \text{and } j \in I_A \cap (I_{2d} \setminus \{\underline{x}_j : x_{j\,2} = 0\}) \\ \begin{cases} \underline{U}_i - \underline{U}_j = -\underline{\underline{\epsilon}}^{\infty} \cdot 2d\underline{e}_1 & \text{for } i \in I_0 \cap \{\underline{x}_i : x_{i\,2} = 0\} \\ \underline{A}_i - \underline{A}_j = 0 & \text{and } j \in I_{2d} \cap \{\underline{x}_j : x_{j\,2} = 0\} \end{cases} \end{cases} \tag{A.4b}$$

5. Defining the homogeneous boundary strain loading vector $\{\epsilon\} = \left\{\epsilon_1^{\infty} \quad \epsilon_2^{\infty} \quad \epsilon_3^{\infty} \quad \right\}^T$ (see Fig. 14(a) for orientation), three elementary loadings are constituted: $\{\epsilon\}^1 = \left\{1 \quad 0 \quad 0\right\}^T$, $\{\epsilon\}^2 = \left\{0 \quad 1 \quad 0\right\}^T$ and $\{\epsilon\}^3 = \left\{0 \quad 0 \quad 1\right\}^T$.
   Linear elastic problems are solved (Fig. 14(b)) and equivalent homogeneous boundary stress loadings $\{\sigma\} = \left\{\sigma_1^{\infty} \quad \sigma_2^{\infty} \quad \sigma_3^{\infty}\right\}^T$ are deduced for the three loadings.
6. The two interaction integrals are computed to evaluate the two stress intensity factors. G-θ method is applied for five domains of integration to check its consistency. The range of variation is found to be less than 0.025% in average for the finest mesh studied.
7. Value of the six functions $\mathcal{F}_i^p$, $i = 1, 2, 3$, $p = I$, II are finally deduced by solving the two linear systems:

$$\begin{bmatrix} \sigma_1^{\infty\,1} & \sigma_1^{\infty\,2} & \sigma_1^{\infty\,3} \\ \sigma_2^{\infty\,1} & \sigma_2^{\infty\,2} & \sigma_2^{\infty\,3} \\ \sigma_3^{\infty\,1} & \sigma_3^{\infty\,2} & \sigma_3^{\infty\,3} \end{bmatrix} \cdot \begin{pmatrix} \mathcal{F}_1^p \\ \mathcal{F}_2^p \\ \mathcal{F}_3^p \end{pmatrix} = \frac{1}{\sqrt{2d}} \begin{pmatrix} K_p^1 \\ K_p^2 \\ K_p^3 \end{pmatrix} \qquad \text{for } p = \{I, II\} \tag{A.5}$$

Appendix A.3. Numerical results

Evolution with angle α of functions $\mathcal{F}_i^p$ taken for equally spaced values of $\frac{c}{d}$ are given Fig. A.14

Evolutions are difficult to predict with analytical model in the whole range considered. This is particularly true for $\frac{c}{d}$ between 0.8 and 1.0 and small value of α, because the two crack tip interact strongly and change deeply the nature of the solution.

Compared to Leblond and Frelat (2014), computations have been led for a wide range of parameters and enables an accurate implementation in the cohesive zone model.

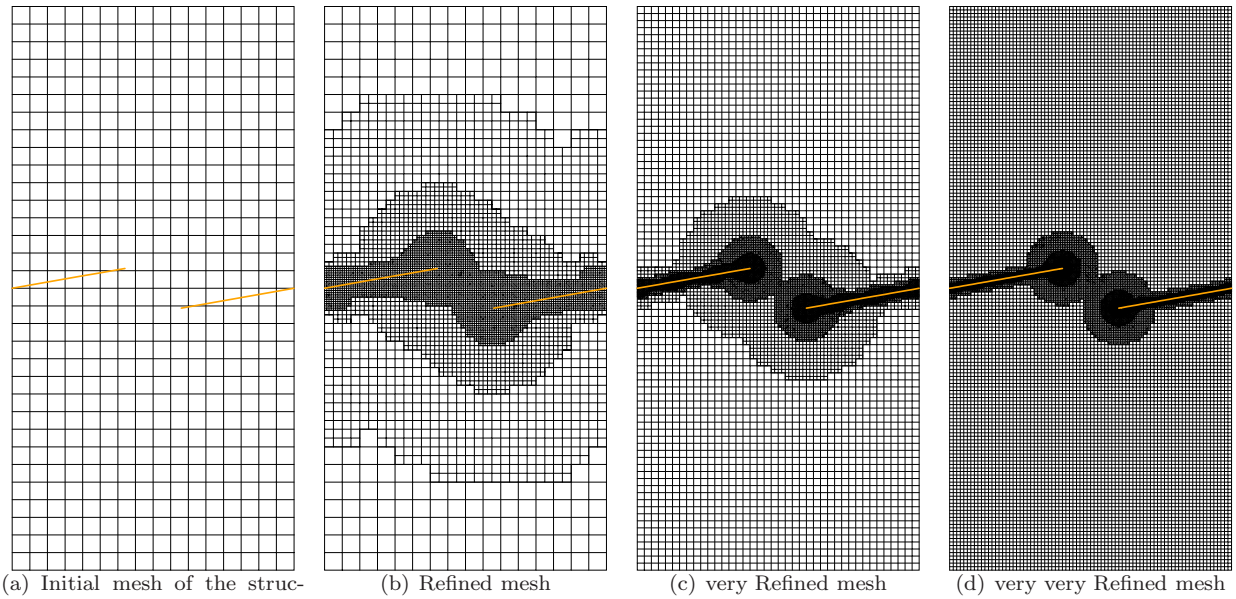

(a) Initial mesh of the structure and of the crack (b) Refined mesh (c) very Refined mesh (d) very very Refined mesh

Figure A.13: Combination of XFEM and hierarchical mesh refinement

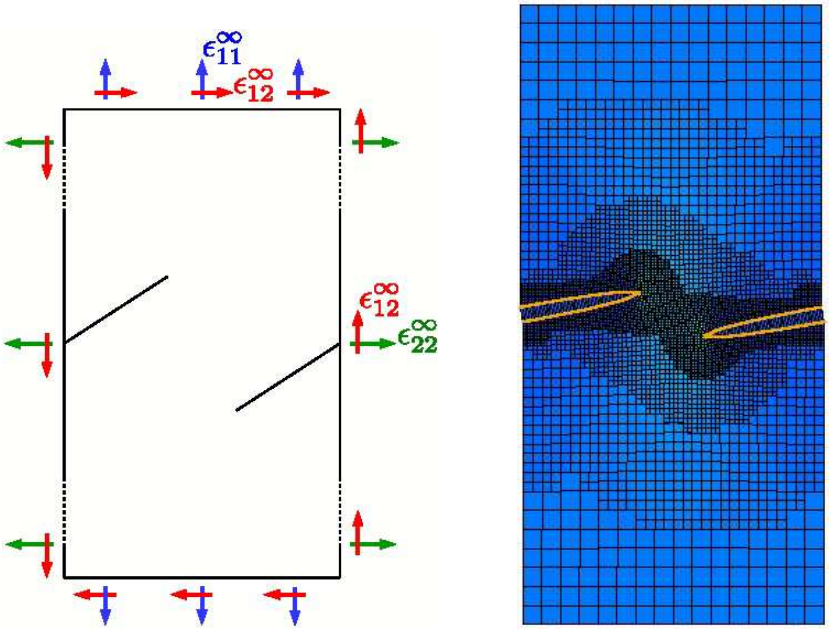

(a) Elementary homogeneous boundary strain loadings

(b) Deformed mesh resulting from the the first loading ϵ_1^{∞}

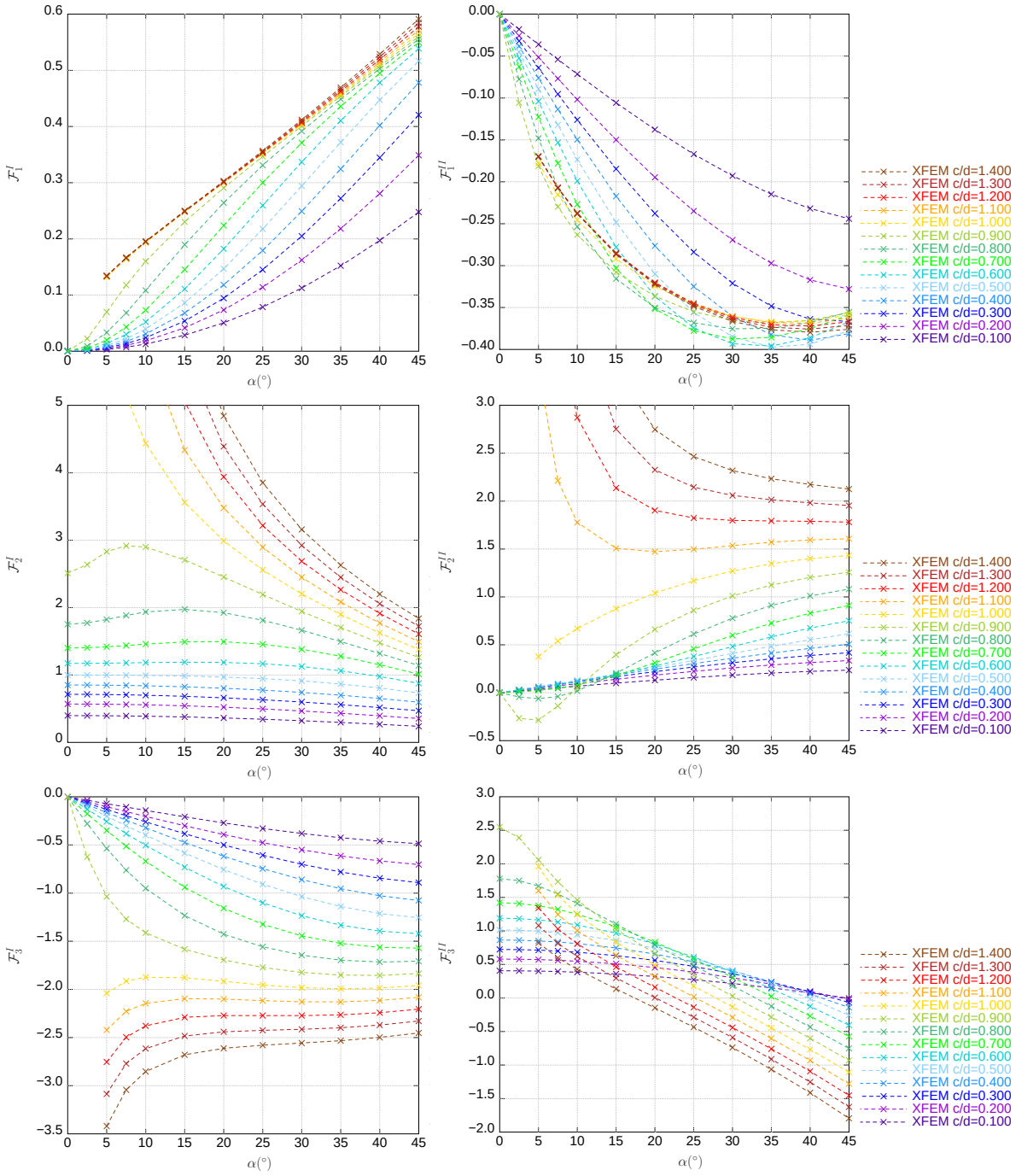

Figure A.14: Functions $\mathcal{F}_i^p\left(\alpha, \frac{c}{d}\right)$